Direct Numerical Simulation of Breaking of Standing Internal Waves

by

Karthik Velakur

A research paper
presented to the University of Waterloo
in partial fulfillment of the
requirement for the degree of
Master of Mathematics
in
Computational Mathematics

Supervisor: Prof. Michael L. Waite

Waterloo, Ontario, Canada, 2014

I hereby declare that I am the sole author of this report. This is a true copy of the report, including any required final revisions, as accepted by my examiners.

I understand that my report may be made electronically available to the public.

Abstract

We use direct numerical simulations to study the evolution of a initially two-dimensional standing internal gravity wave in a 1024^3 periodic computational cube. The numerical method used is a spectral method dealised with Orszag's 2/3 rule. We examine the density field and kinetic energy spectra during and in the immediate aftermath of the breaking of the wave. We also attempt to study the transition in the kinetic energy spectra from the anisotropic k^{-3} buoyancy-range to the isotropic $k^{-5/3}$ inertial-range.

We find that the breaking of the standing wave is initially two-dimensional and accompanied by a steep decline in the total energy of the system and an increase in the dissipation rate. It the aftermath of the breaking, a lot of small scale features are generated. Then, there is also a secondary wave breaking during which the dissipation rate reaches its maximum. We also find a wide k^{-3} buoyancy-range in the kinetic energy spectrum in-between the two breaking events. After the second wave breaking event, we find a wide $k^{-5/3}$ inertial-range spectrum. We also justify the use of Taylor's hypothesis in the experiments of Benielli and Sommeria [1996], where the authors find a f^{-3} frequency spectra in density field, and conclude the presence of a k^{-3} wavenumber spectra in the kinetic energy.

Acknowledgements

I would like to thank my supervisor Prof. Michael Waite for his guidance and support. Our weekly meetings helped me to stay motivated. I would also like to thank Prof. Marek Stastna whose courses helped me understand the fluid dynamics and spectral methods background required for this project.

Thanks also to my friends who made my stay here at Waterloo enjoyable.

This work was made possible by the facilities of the Shared Hierarchical Academic Research Computing Network (SHARCNET:www.sharcnet.ca) and Compute/Calcul Canada.

Table of Contents

List of Figures

Chapter 1

Introduction

Internal gravity waves can occur in the interior of any fluid with a stable density stratification, like the oceans or the atmosphere. The stratification can be due to vertical temperature or salinity gradients, and in either case wave motion can be induced with gravity as the restoring force. The breaking of internal gravity waves is a major source of turbulence in the interior of oceans (Lesieur [2008]). Breaking is observed when the amplitude of the wave become large enough for local overturning to occur. Heavier fluid from underneath in the stratified medium spills over the lighted fluid, and this leads to irreversible mixing and turbulence. In turbulent flow, eddies of different sizes are formed and they interact with each other. The large eddies are due to internal wave activity and contain most of the energy, while the smallest ones are due to isotropic turbulence where energy is dissipated into heat by viscosity. Between these two extremes, the dynamics is a competition between waves and turbulence. This range of length scales is called the buoyancy-range, and it is not very well understood. The smallest scales are characterized by the Kolmogorov theory under an assumption of isotropy, and are known to exhibit a $k^{-5/3}$ power law for the kinetic energy spectrum. For the intermediate anisotropic buoyancy-range, it is generally accepted that a k^{-3} power law holds for the kinetic energy spectrum (Carnevale et al. [2001]).

There have been a number of experimental studies that attempt to study the breaking of internal gravity waves in order to understand the buoyancy-range of turbulence (Benielli and Sommeria [1996], Benielli and Sommeria [1998]). In these studies, internal waves are induced in a cubic tank with a stratified fluid by oscillating it vertically. Physically it is difficult to obtain the wavenumber energy spectra, but it is possible to obtain the frequency spectra of the density of the fluid at fixed locations the tank. In order to relate these spectra, the authors propose a simple relationship between the spatial wavenumber and temporal frequency.

A number of numerical studies (Bouruet-Aubertot et al. [1996], Bouruet-Aubertot et al. [1995], Carnevale et al. [2001]) have been performed to study the breaking of internal waves and the kinetic energy spectra. But all of these have either been (a) two-dimensional which is not suitable to model the highly anisotropic buoyancy-range, or (b) a low resolution large eddy simulation, which is not as accurate as a direct numerical simulation which faithfully represents all scales in the system.

In this report, we attempt to characterize the breaking of an initially smooth standing internal gravity wave using full direct numerical simulations of the nonlinear Navier-Stokes equations under the Boussinesq approximation. We will study the evolution of the density field and make observations about the kind of structures that formed in the field. We will also study the vertical wavenumber spectra and try to relate it to the frequency spectra of the density in the middle of our computational domain.

The Chapters 2 and 3 contain the relevant fluid dynamics and numerical methods background that is needed to understand the problem at hand. Chapter 4 contains the results of the simulation and interpretation of results. We summarize the results and discuss conclusions in Chapter 5.

Chapter 2

Fluid dynamics background

2.1 Introductory theory of turbulence

Turbulence is the state of fluid motion that is chaotic and and accompanied by apparently unpredictable three dimensional vorticity. When it is present, it is a dominant phenomena, resulting in increased energy dissipation, mixing, heat transfer and drag (Lesieur [2008]). Turbulence is ubiquitous: like the smoke rising from a cigarette, exhaust from an automobile all all geophysical flows like ocean and atmospheric currents. One often hears the term during air travel, and it signals a bumpy ride.

The study of turbulence is widely acknowledged to be one the most intriguing, intractable and important problems of classical physics. It is a subject studied by many of the greatest physicists and mathematicians of the 19th and 20th centuries, yet we do not possess a complete understanding of how or why it occurs, nor can we predict turbulent behaviour accurately. At one point, it was thought there might be a universal theory of turbulence, along the lines of the kinetic theory of gases, that averages out the apparently random motions of the fluid and gives us a non-random, macroscopic, statistical model (Davidson [2004]). However, even after a century of concerted research effort, such a theory has not been found. What has emerged are a few universal features of turbulence, like Kolmogorov's theory for small scale turbulence (1941), and the law of the wall for turbulent flow near a smooth wall first propsed by von Kármám (1930).

2.1.1 Description of turbulence

The Navier-Stokes equations are universally accepted as the most general descriptors of the physics of all Newtonian fluid flows, including turbulent ones, within the confines of the continuum hypothesis. For an incompressible fluid (with a constant density), the equations are written as

$$\rho\left(\frac{\partial \boldsymbol{u}}{\partial t} + \boldsymbol{u}\cdot\nabla\boldsymbol{u}\right) = -\nabla p + \mu\nabla^2\boldsymbol{u} + \boldsymbol{f}_b, \tag{2.1}$$

$$\nabla\cdot\boldsymbol{u} = 0. \tag{2.2}$$

In these equations

- $\mathbf{u}(x,y,z) = (u(x,y,z), v(x,y,z), w(x,y,z))$ is the velocity field in the $\boldsymbol{x} = (x,y,z)$ directions respectively,
- $p(x,y,z)$ is the fluid pressure,
- $\rho(x,y,z)$ is the fluid density,
- μ is the dynamic viscosity, and $\nu = \mu/\rho$ is the kinematic viscosity,
- $\boldsymbol{f}_b$ is the body force per unit volume.

The Navier-Stokes equations (2.1-2.2) are nonlinear and difficult to solve. By introducing some simplifying and often physically unrealistic assumptions, exact solutions can be obtained, but often these are of little value. Early descriptions of turbulence thus were based mainly on experimental observations. Osborne Reynolds was the first to formally study the conditions under which the flow of fluid transitions from laminar to turbulent flow. His observations of flow in pipes led him to define a dimensionless parameter, now called the *Reynolds number* Re,

$$\mathrm{Re} = \frac{\rho U L}{\mu} = \frac{U L}{\nu} \tag{2.3}$$

that characterizes flow behaviour in this situation. Here, ρ and μ are the fluid density and dynamic viscosity respectively. U and L are the typical velocity and length scales of the flow. What Re quantifies is the ratio of the inertial forces to the viscous forces and the

relative importance of these types of forces for the given flow conditions. Note that this can be realized by scaling

$$\tilde{\boldsymbol{x}} = \frac{\boldsymbol{x}}{L}, \quad \tilde{t} = t\frac{U}{L}, \quad \tilde{p} = \frac{p}{\rho U^2}, \quad \tilde{\boldsymbol{u}} = \frac{\boldsymbol{u}}{U}, \tag{2.4}$$

and writing (2.1) as

$$\frac{\partial \tilde{\boldsymbol{u}}}{\partial t} + \tilde{\boldsymbol{u}} \cdot \nabla \tilde{\boldsymbol{u}} = -\nabla \tilde{p} + \frac{1}{\mathrm{Re}} \nabla^2 \boldsymbol{u} + \tilde{\boldsymbol{f}}_b, \tag{2.5}$$

and realizing how the parameter Re controls the dynamics between the inertial forces arising from $\boldsymbol{u} \cdot \nabla \boldsymbol{u}$ and the dissipative viscous forces arising from $\mu \nabla^2 \boldsymbol{u}$. For small values of Re the flow remains laminar. As Re increases and reaches a certain critical value, small disturbances can cause the flow to become unstable. For very large values ($> 10^4$), the turbulence is fully developed and it is the dominant mechanism in the flow. Under fully developed turbulence, fluid particles move erratically and there is a lot of mixing (Avila et al. [2011]).

Some physical attributes of turbulence that summarize the descriptions of turbulent flow are

- Irregularity. Turbulent flow is disorganized, chaotic, and seemingly random. This is why a statistical approach can also be used to understand it.
- Nonrepeatability. The evolution of turbulence is sensitive to initial conditions, but after a certain amount of time it shows non-repeatable fluctuations.
- Dissipation. Both diffusion and dissipation are enhanced by turbulence.
- Rotationality. Turbulent flows are characterized by strong three dimensional vorticity generation by vortex stretching.

2.1.2 Richardson's energy cascade

The Richardson (Richardson [1926]) cascade is a phenomenological way to explain the transfer of energy from the largest scales in the system to the smaller ones. A brief explanation of this idea as presented in Davidson [2004] follows.

Statistically stationary turbulent flow can be considered to be composed of a mean flow and a random fluctuating component. At a location $\boldsymbol{x}$, the velocity $\boldsymbol{u}$ can be assumed to be

$$\boldsymbol{u}(\boldsymbol{x}, t) = \bar{\boldsymbol{u}}(\boldsymbol{x}) + \boldsymbol{u}'(\boldsymbol{x}, t) \tag{2.6}$$

where $\bar{\boldsymbol{u}}$ is the time averaged mean velocity, and $\boldsymbol{u}'$ is the random component. We consider the turbulence when $\mathrm{Re} = UL/\nu$ is large, where U is the typical value of $\boldsymbol{u}'$ and L is the typical size of large scale turbulence eddies. The largest eddies are accompanied by smaller eddies with a wide range of sizes. The dissipation rate is given by

$$\varepsilon = 2\nu \|\boldsymbol{S}\|^2 \tag{2.7}$$

where $\boldsymbol{S}$ is the strain rate tensor whose elements are of the form

$$S_{ij} = \frac{1}{2}\left(\frac{\partial u_i}{\partial x_j} + \frac{\partial u_j}{\partial x_i}\right), \quad i, j = 1, 2, 3. \tag{2.8}$$

Hence, we expect maximum dissipation in the areas where the shear, or the instantaneous gradient in velocity is largest.

This led Richardson to believe that the dissipation of mechanical energy is concentrated in the smallest eddies, where the shear stress is large. The largest eddies are created by instabilities in the mean flow, and are themselves subjected to inertial instabilities leading to their break up into smaller eddies. The life-span of a typical eddy is of the same order of its so-called turn-over time L/U (confirmed by experimental evidence). The smaller eddies further break up into even smaller eddies, and so on. Thus, there is a continual cascade of energy from larger to smaller scales. It is important to note that viscosity is not important at this stage, because $\mathrm{Re} = UL/\nu$ is large, and the viscous stresses acting on these eddies are negligible. This whole process is driven by inertial forces, until the size of the eddy becomes so small that Re is of the order of unity. At this scale, viscous forces are significant, and dissipation has to be accounted for. So we can visualize a picture of large scale eddies being created by mean flow, these eddies breaking into smaller ones through a series of inviscid instabilities, and energy being destroyed by viscosity only in the final stages where Re is of the order of unity.

We can now perform some heuristic calculations to determine the smallest scales in the turbulent cascade. We represent U and v as the typical velocities associated with the largest and smallest eddies respectively, and L and η as the typical length scale of the largest and smallest eddies respectively. We can then estimate the rate of energy per unit

mass (which has units $\mathrm{m}^2\ \mathrm{s}^{-1}$) passed down by the energy cascade as a function of the turn over time L/U

$$\Pi \sim \frac{U^2}{L/U} = \frac{U^3}{L}. \tag{2.9}$$

This is an estimation based on dimensional analysis. Similarly, the rate of dissipation at the smallest scales is

$$\varepsilon \sim \nu S_{ij} S_{ij} \sim \nu \frac{v^2}{\eta^2}. \tag{2.10}$$

When conditions are statistically steady, the rate of the energy cascade must match exactly the dissipation of energy at small scales. This is because energy is not accumulated at some intermediate scale during fully developed turbulence. Hence,

$$\frac{U^3}{L} \sim \nu \frac{v^2}{\eta^2}. \tag{2.11}$$

However, we also know that at the smallest scales the Re, based on v and η is of the order of unity

$$\frac{v\eta}{\nu} \sim 1. \tag{2.12}$$

Combining (2.11) and (2.12), we find

$$\eta \sim L\mathrm{Re}^{-\frac{3}{4}} \quad \text{or} \quad \eta \sim \left(\frac{\nu^3}{\varepsilon}\right)^{\frac{1}{4}}, \tag{2.13}$$

and

$$v \sim U\mathrm{Re}^{-\frac{1}{4}} \quad \text{or} \quad v \sim (\nu\varepsilon)^{\frac{1}{4}}, \tag{2.14}$$

where $\mathrm{Re} = UL/v$ is based on the largest scale eddies. The quantity η is called the *Kolmogorov dissipation scale*, while L is called the *integral scale*.

A typical lab-scale water channel experiment will have $\mathrm{Re} \sim 10^4$, $L \sim 10$ cm, $U \sim 10$ cm s^{-1}, giving $\eta \sim 0.1$ mm and $v \sim 1$ cm s^{-1}. Or for a typical wind tunnel might have, $\mathrm{Re} \sim 10^5$, $L \sim 1$ m, $U \sim 1$ m s^{-1} giving, $\eta \sim 0.2$ mm and $v \sim 5$ cm s^{-1}. So much of the energy dissipated will be contained in eddies less than a millimeter in size!

2.1.3 Kolmogorov's theory of 1941

In 1941 the Russian statistician Andrey Kolmogorov published three papers (in Russian) (Kolmogorov [1941c], Kolmogorov [1941a], Kolmogorov [1941b]) that form some of the most important and most quoted results in turbulence theory. These results are popularly called the "K41 theory" to distinguish them from his later work, called the "K61 theory" Kolmogorov [1962]. Kolmogorov originally stated his theory by basing them on two "universality assumptions". Frisch (Frisch [1995]) provides a more easily understood explanation of this theory, and that is what we will state here. The starting point is the a set of three hypothesis:

Hypothesis 1 *In the $Re \to \infty$ limit, all possible symmetries of the Navier-Stokes equations, usually broken by the (physical) mechanisms producing turbulence, are restored in a statistical sense at small scales and away from boundaries.*

Hypothesis 2 *Under the assumptions as above, turbulent flow is self similar at small scales; i.e., it possesses a unique scaling exponent h such that*

$$\delta \boldsymbol{u}(\boldsymbol{x}, \lambda \boldsymbol{l}) = \lambda^h \delta \boldsymbol{u}(\boldsymbol{x}, \boldsymbol{l}), \quad \forall \lambda \in \mathbb{R}_+, \quad \boldsymbol{x} \in \mathbb{R}^3, \tag{2.15}$$

with increments $\boldsymbol{l}$ and $\lambda \boldsymbol{l}$ small compared with the integral scale.

Hypothesis 3 *Again, under the same assumption as in Hypothesis 1, turbulent flow has a finite, nonvanishing mean rate of dissipation per unit mass, ε.*

The small scales referred to in Hypotheses 1 and 2 are associated with length scales much smaller than the integral scale. One way to interpret this small-scale homogeneity is in the context of velocity increments

$$\delta \boldsymbol{u}(\boldsymbol{x}, \boldsymbol{l}) \equiv \boldsymbol{u}(\boldsymbol{x} + \boldsymbol{l}) - \boldsymbol{u}(\boldsymbol{x}) \tag{2.16}$$

and the requirement that statistics of these increments be invariant under arbitrary translations $\boldsymbol{r}$ for steady flow,

$$\langle \delta \boldsymbol{u}(\boldsymbol{x} + \boldsymbol{r}, \boldsymbol{l}) \rangle = \langle \delta \boldsymbol{u}(\boldsymbol{x}, \boldsymbol{l}) \rangle, \tag{2.17}$$

where $\langle \cdot \rangle$ denotes any generic averaging procedure. The requirement of being "away from boundaries" makes sense in the same context, because homogeneity and isotropy cannot

be expected to hold in the vicinity of solid boundaries. Hypothesis 2 establishes a vector self similarity relation (2.15) in velocity increments, where λ and h are scalars and the spatial increment $\boldsymbol{l}$ and positive multiplier are small compared with the integral scale. Also the power law representation found in (2.15) is typical of fractal attractors of differential dynamical systems and their trajectories appear same on all scales. Finally, Hypothesis 3 agrees with experimental observations. Sreenivasan (Sreenivasan [1984]) performed an experiment, and measured $\varepsilon L/U^3$, the nondimensionalized dissipation rate, where L and U are the integral scale and r.m.s. turbulence velocity fluctuation for a range of Re values. He found that this nondimensional dissipation is independent of Re.

Kolmogorov's 2/3 law. *In a turbulent flow at very high Reynolds number, the mean-square velocity increment* $\mathcal{E} = \langle(\delta\boldsymbol{u}(\boldsymbol{l}))^2\rangle$ *between two points separated by a distance* $\boldsymbol{l}$ *behaves approximately as the two-thirds power of the distance.*

As we have already discussed, based on Hypothesis 2, $|\boldsymbol{l}| = l$ is much smaller than the integral scale. The 2/3 law holds specifically in the inertial subrange of the energy spectrum, where viscosity is unimportant, i.e., viscous forces are dominated by inertial forces. This corresponds to a sufficiently high Re so that at large scales, flow is dominated by inertial effects. This means that at smaller scales, the turbulence statistics are only dependent on the length l and dissipation rate ε.

To explain Kolmogorov's 2/3 law, we first need to realize that the quantity $\langle(\delta\boldsymbol{u}(\boldsymbol{l}))^2\rangle = \langle(\boldsymbol{u}(\boldsymbol{x}+\boldsymbol{l}) - \boldsymbol{u}(\boldsymbol{x}))^2\rangle$ is associated with kinetic energy of fluctuations, and has dimensions L^2/T^2. Also, ε has dimensions L^2/T^3, and so the only combination of ε and l to form $\mathcal{E}$ are

$$\mathcal{E} = C\varepsilon^{2/3}l^{2/3}, \tag{2.18}$$

where C is a universal constant.

The $k^{-5/3}$ energy spectrum. We can now use (2.18) to derive the Kolmogorov $k^{-5/3}$ inertial-range scaling of the turbulent energy spectrum. The fraction of energy $\mathrm{d}\mathcal{E}$ contained in the eddies with wavenumbers ranging from k to $k + \mathrm{d}k$ is $\mathrm{d}\mathcal{E} = E(k)\,\mathrm{d}k$. It follows that the cumulative energy corresponding to all wavenumbers higher than an arbitrary k is

$$\mathcal{E}(k) = \int_k^\infty \mathrm{d}\mathcal{E} = \int_k^\infty E(k)\,\mathrm{d}k. \tag{2.19}$$

Note that, the wavenumber k associated with a length scale r is $k = 1/r$ (up to a scaling constant, depending on the chosen Fourier representation); and because of the integral scale and (2.13), the extremal values of k are $k_{\min} \sim 1/L$ and $k_{\max} \sim \varepsilon^{1/4}\nu^{-3/4}$.

Frisch (Frisch [1995]) shows, that under general circumstances $E(k)$ must satisfy

$$E(k) \propto k^{-n}, \quad 1 < n < 3. \tag{2.20}$$

Hence, substituting (2.20) into (2.19) gives

$$\begin{aligned} \mathcal{E} &\simeq \int_k^\infty k^{-n}\,\mathrm{d}k \\ &= -\frac{1}{1-n}k^{-n+1} \\ &\simeq -\frac{1}{1-n}E(k)k. \end{aligned} \tag{2.21}$$

For the range of values of n permitted in (2.20),

$$C_n \equiv -\frac{1}{1-n} > 0,$$

and we can write,

$$C_n E(k)k = \mathcal{E}(k) = C\varepsilon^{2/3}k^{-5/3}.$$

Rearranging gives,

$$E(k) = C_K\varepsilon^{2/3}k^{-5/3}, \tag{2.22}$$

the well-known result for the Kolmogorov inertial-range spectrum. Here C_K is the Kolmogorov constant, and it is experimentally determined to be about 1.5 for three-dimensional spectra (Sreenivasan [1995]).

2.2 Internal gravity waves

2.2.1 The Boussinesq approximation

The Navier-Stokes equations, which arise from the Newton's second law of motion, are the most general description of fluid motion. Along with the equations for conservation of mass and energy and well formulated boundary conditions, they can model fluids accurately. For geophysical fluid flows, characterized by accounting for the rotation of fluid due to

planetary rotation, and stratification or layering of the fluid according to density, some approximations can be adopted that leads to a simplification of the Navier-Stokes equations. These approximations, attributed to Boussinesq (Boussinesq [1903]), are summarized by Spiegel and Veronis (Spiegel and Veronis [1960]) by the following two statements: "(1) The fluctuations in density which appear with the advent of motion result principally from thermal (as opposed to pressure effects). (2) In the equations for the rate of change of momentum and mass, density variations may be neglected except when they are coupled to the gravitational acceleration in the buoyancy force."

Under the Boussinesq approximation, evolution equations may be written as

$$\frac{\partial \boldsymbol{u}}{\partial t} + \boldsymbol{u} \cdot \nabla \boldsymbol{u} + \frac{1}{\rho_0} \nabla p - \frac{\rho'}{\rho_0} \boldsymbol{g} + 2\boldsymbol{\Omega} \times \boldsymbol{u} = \nu \nabla^2 \boldsymbol{u} \tag{2.23}$$

$$\nabla \cdot \boldsymbol{u} = 0 \tag{2.24}$$

$$\frac{\partial \rho'}{\partial t} + \boldsymbol{u} \cdot \nabla \rho' = \frac{\partial \bar{\rho}}{\partial z} w + \kappa \nabla^2 \rho' \tag{2.25}$$

where in addition to the vaiables from the Navier-Stokes equations (2.1-2.2), we have the following dimensional variables:

- $\rho'(x, y, z)$ is a perturbation density, and $\bar{\rho}(z)$ is a background density profile. ρ_0 is the average of $\bar{\rho}(z)$ over z. The total density is given by $\rho = \bar{\rho} + \rho'(x, y, z, t)$. We also assume the perturbation is small, $\rho'/\rho_0 \ll 1$.
- $\boldsymbol{g} = (0, 0, -g)$ is the acceleration due to gravity.
- $\boldsymbol{\Omega}$ is the angular velocity of the co-ordinate system. Typically, it is due to the rotation of the earth.
- κ is the constant molecular diffusivity.

The vector equation (2.23) and equations (2.24), (2.25) are a coupled system of partial differential equations in five unknowns, $\boldsymbol{u}$, p, and ρ'. Equation (2.23) is the modified Navier-Stokes momentum equation with the Boussinesq approximation, where we can see that when conserving momentum, we disregard the change in density, except when ρ' is multiplied by g. The term $\rho' g/\rho_0$ is called the buoyancy term, and in flows involving buoyant convection its magnitude is of the same order as the vertical acceleration $\partial w/\partial t$ or the viscous term $\nu \nabla^2 w$. Equation (2.24) is the continuity equation for an incompressible fluid, which means that the relative density changes of a fluid particle $\rho^{-1}(D\rho/Dt)$ are small compared to velocity gradients that constitute $\nabla \cdot \boldsymbol{u}$. This excludes scenarios like

high speed gas flows where the Mach number is large, or in large scale flows where where the density changes in the vertical direction is of the order $c^2/g \approx 10$ km, c being the speed of sound in the air. For our application of the study of turbulence in a stratified medium, these constraints hold. Finally, equation (2.25) stems from the energy equation, which reduces to an equation for the perturbation density ρ'. Using the equation of state for an ideal gas, (2.25) can also be cast in terms of an equation in terms of perturbation temperature T'.

For a detailed explanation of how these equations are derived, one can refer to [Kundu et al., 2011, Chapter 4], or Spiegel and Veronis [1960].

2.2.2 Stratification

As stated in Section 2.2.1, problems in geophysical fluid dynamics concern fluid motions with one or both of planetary rotation and *stratification*. A stratified fluid will tend to align itself, under gravity, so that higher densities are found under lower densities. Such vertical stratification is a naturally occurring phenomenon in both the oceans and the atmosphere. For example, in the ocean, the average temperature is about $T = 10\,^{\circ}\mathrm{C}$ near the surface and typical salinity is $S = 3.47\%$, which corresponds to a density of $\rho = 1028\,\mathrm{kg/m^3}$ at surface pressure, and variations in the density rarely exceed $3\,\mathrm{kg/m^3}$. In the lowest layer of the atmosphere called the trophoshere (which extends to a height of 10 km above sea level), where most of the weather patterns are confined, the density variation is no more than 5%.

Let us start by considering an incompressible stratified fluid in static equilibrium, i.e., a fluid at rest because of the lack of lateral forces. The stratification is purely vertical with a background density profile of $\bar{\rho}(z)$, and the fluid is horizontally homogeneous. If we were to displace a fluid parcel at a height z with density $\bar{\rho}(z)$ to a height $z+h$, where the ambient density is $\bar{\rho}(z+h)$, the parcel would retain it density because of incompressibility, and experience a buoyancy force equal to

$$g\left[\bar{\rho}(z+h) - \bar{\rho}(z)\right] V,$$

where V is the volume of the parcel. Newton's first law of motion (force equals mass times acceleration) then tell us that

$$\bar{\rho}(z)\, V \frac{\mathrm{d}^2 h}{\mathrm{d}t^2} = g\left[\bar{\rho}(z+h) - \bar{\rho}(z)\right] V. \tag{2.26}$$

One of the assumptions that is made in the Boussinesq approximation is that density perturbations are small, and this allows us to write $\bar{\rho}(z)$ on the left as ρ_0, and use Taylor expansion to write

$$\bar{\rho}(z+h) - \bar{\rho}(z) \approx \frac{\mathrm{d}\bar{\rho}}{\mathrm{d}z} h.$$

Equation (2.26) hence reduces to

$$\frac{\mathrm{d}^2 h}{\mathrm{d}t^2} - \frac{g}{\rho_0}\frac{\mathrm{d}\bar{\rho}}{\mathrm{d}z} h = 0, \tag{2.27}$$

which shows that one of two things can occur, depending on if the coefficient $-(g/\rho_0)\,\mathrm{d}\bar{\rho}/\,\mathrm{d}z$ is positive or negative. If it is positive (i.e., $\mathrm{d}\bar{\rho}/\,\mathrm{d}z < 0$ which means denser fluid is under lighter fluid), then the solution is (2.27) is a simple oscillator with a frequency N given by

$$N^2 \equiv -\frac{g}{\rho_0}\frac{\mathrm{d}\bar{\rho}}{\mathrm{d}z}. \tag{2.28}$$

This means that the fluid parcel when displaced upwards to a region of higher density, sinks due to a downward restoring force, due to the inertia reaches the region with lower density and is pushed back up again due to the buoyancy. This oscillation is sustained about the equilibrium position. The quantity $N(z)$ defined by the square root of the expression on the right of (2.28) is important because it defines the buoyancy frequency. It is commonly called the Brunt-Väisälä frequency, after David Brunt and Vilho Väisälä, who were the first scientists to highlight the importance of this frequency in stratified fluids.

On the other hand, if the coefficient is negative (i.e., $\mathrm{d}\bar{\rho}/\,\mathrm{d}z > 0$ corresponding to heavier fluid on top of lighter fluid), the solution of (2.27) shows exponential growth. Physically, this means that a fluid parcel that is displaced upward will be surrounded by heavier fluid, and it is pushed farther and farther away by buoyancy, setting into motion the process by which the fluid tries to stabilize itself so that lighter fluid is above heavier fluid.

2.2.3 Internal gravity waves

We shall now demonstrate that a fluid that is vertically and stably stratified can exhibit waves in its interior. As discussed in Section 2.2.2, gravity (or buoyancy) acts as the restoring force. A common example of internal gravity waves is the oceanic phenomenon of "dead water" in Norwegian fjords which causes sizable drag on passing ships (Gill [1982]). The phenomenon was a mystery until it was explained as being due to the formation of

internal waves at the interface of a shallow layer of light water sitting on denser water. In fact the existence of these waves is not restricted to just the case of two layer and one interface. For three fluid layers of different densities and two interfaces, two wave modes are possible, under the condition that the middle layer is thin enough to let energy pass from the top to the bottom. In the limiting case of a continuously stratified fluid, an infinite number of modes are possible. These waves are dispersive (i.e., its phase speed and group speed are different). They can also propagate in either the vertical or the horizontal direction.

Following the method outlined in Kundu et al. [2011], we will derive some results about internal gravity waves using linear theory. The assumptions that we make are: (1) There is no ambient rotation, or it is small enough to to ignored. (2) The domain is infinite in all directions. (2) There is no dissipative mechanism of any kind, i.e., the motion is effectively inviscid. (4) The fluid motions are small. The very last assumption allows us to linearize the governing equations. Under these assumptions, the governing set of equations (2.23-2.25) may be written as

$$\frac{\partial u}{\partial t} = -\frac{1}{\rho_0}\frac{\partial p}{\partial x}, \quad \frac{\partial v}{\partial t} = -\frac{1}{\rho_0}\frac{\partial p}{\partial y}, \quad \frac{\partial w}{\partial t} = -\frac{1}{\rho_0}\frac{\partial p}{\partial z} - \frac{\rho g}{\rho_0}, \tag{2.29}$$

$$\frac{\partial u}{\partial x} + \frac{\partial v}{\partial y} + \frac{\partial w}{\partial z} = 0, \tag{2.30}$$

$$\frac{\partial \rho'}{\partial t} + w\frac{\partial \bar{\rho}}{\partial t} = 0, \tag{2.31}$$

respectively. The set (2.29) are the same as the linear momentum equations (2.23) without the nonlinear advection term and the dissipation term; (2.30) is the incompressible continuity equation; and (2.31) is the density equation (2.25) without the nonlinear term and dissipation term.

There are five unknowns that we are solving for in system (2.29-2.30), viz. (u,v,w,p,ρ). We already know that when the fluid is immobile (i.e. under hydrostatic balance), the density profile is just a function of z, $\bar{\rho}(z)$. The quiescent pressure distribution is similarly a function of z, say $\bar{p}(z)$. The equation for vertical acceleration in (2.29) allows us to relate the quiescent pressure and density by the relation

$$0 = -\frac{1}{\rho_0}\frac{\mathrm{d}\bar{p}}{\mathrm{d}z} - \frac{\bar{\rho} g}{\rho_0}. \tag{2.32}$$

When motion develops, the pressure will change relate to this quiescent value

$$p = \bar{p}(z) + p'. \tag{2.33}$$

Hence (2.29) can be written as

$$\frac{\partial u}{\partial t} = -\frac{1}{\rho_0}\frac{\partial p'}{\partial x}, \quad \frac{\partial v}{\partial t} = -\frac{1}{\rho_0}\frac{\partial p'}{\partial y}, \quad \frac{\partial w}{\partial t} = -\frac{1}{\rho_0}\frac{\partial p'}{\partial z} - \frac{\rho' g}{\rho_0}. \tag{2.34}$$

Now, we rewrite (2.31) using a constant Brunt-Väisälä frequency N (2.28) as

$$\frac{\partial \rho'}{\partial t} - \frac{N^2 \rho_0}{g} w = 0. \tag{2.35}$$

The system of equations we need to solve is now equations (2.34), (2.30), and (2.35). We can now obtain an equation involving only p' and w by taking the time derivative of (2.30) and using the horizontal momentum equations in (2.34) to eliminate u and w. The result will be

$$\frac{1}{\rho_0}\left(\frac{\partial^2}{\partial x^2} + \frac{\partial^2}{\partial y^2}\right) p' = \frac{\partial^2 w}{\partial z\, \partial t}. \tag{2.36}$$

Another relation between p' and w can be obtained by eliminating ρ' from the vertical momentum equation in (2.34) and (2.35)

$$\frac{1}{\rho_0}\frac{\partial^2 w}{\partial t \partial z} = -\frac{\partial^2 w}{\partial t^2} - N^2 w. \tag{2.37}$$

Finally, p' can be eliminated by operating by $\partial^2/\partial x^2 + \partial^2/\partial y^2$ on (2.37) to obtain an equation in w

$$\frac{\partial^2}{\partial t^2}\nabla^2 w + N^2\left(\frac{\partial^2}{\partial x^2} + \frac{\partial^2}{\partial y^2}\right) w = 0. \tag{2.38}$$

We are now ready to obtain the dispersion relation which relates the angular frequency ω and the wavenumber $\boldsymbol{K} = (k, l, m)$. We do so by seeking a wave solution to (2.38) of the form

$$w = \hat{w}\ \mathrm{e}^{\mathrm{i}\,(kx+ly+mz-\omega t)}. \tag{2.39}$$

Substituting (2.39) into (2.38) leads to the dispersion relation

$$\omega^2 = \frac{k^2 + l^2}{k^2 + l^2 + m^2} N^2. \tag{2.40}$$

Alternatively, (2.40) can be obtained by assuming wave mode solutions of the form

$$\begin{pmatrix} u \\ v \\ w \\ \rho' \\ p' \end{pmatrix} = \begin{pmatrix} \hat{u} \\ \hat{v} \\ \hat{w} \\ \hat{\rho}' \\ \hat{p}' \end{pmatrix} \mathrm{e}^{\mathrm{i}\,(kx+ly+mz-\omega t)}, \tag{2.41}$$

and writing the system (2.34), (2.30), and (2.35) as

$$\begin{pmatrix} -\mathrm{i}\omega & 0 & 0 & -\frac{\mathrm{i}k}{\rho_0} & 0 \\ 0 & -\mathrm{i}\omega & 0 & -\frac{\mathrm{i}l}{\rho_0} & 0 \\ 0 & 0 & -\mathrm{i}\omega & \frac{g}{\rho_0} & -\frac{\mathrm{i}m}{\rho_0} \\ 0 & 0 & -\frac{\rho_0 N^2}{g} & \mathrm{i}\omega & 0 \\ \mathrm{i}k & \mathrm{i}l & \mathrm{i}m & 0 & 0 \end{pmatrix} \begin{pmatrix} \hat{u} \\ \hat{v} \\ \hat{w} \\ \hat{\rho}' \\ \hat{p}' \end{pmatrix} = \begin{pmatrix} 0 \\ 0 \\ 0 \\ 0 \\ 0 \end{pmatrix}. \tag{2.42}$$

A non trivial solution of this system exists if and only if the determinant of the matrix in (2.42) is zero. Setting the determinant to zeros yeilds the same expression (2.40).

For a two dimensional problem in the x-z plane we set $l = 0$ in (2.40). No generality is lost because the medium is horizontally isotropic, and k will represent the entire horizontal wavenumber. We obtain

$$\omega = \frac{kN}{\sqrt{k^2 + m^2}} = N\,\cos\,\theta, \tag{2.43}$$

where $\theta = \tan^{-1}(m/k)$ is the angle between the phase velocity vector $\boldsymbol{c}$ (and therefore $\boldsymbol{K}$) and the horizontal direction. Immediately, certain interesting observations can made with regard to the angular frequency from the expression (2.43). First, the frequency of internal waves in a stratified fluid depends only on the *direction* of the wavenumber vector and not its magnitude. Second, the frequency is bounded by the range $0 < \omega < N$, indicating that N is the maximum possible frequency of internal gravity waves in a stratified fluid.

The dispersion relation (2.43) also allows us to obtain the phase velocity ($\boldsymbol{c}$),

$$\boldsymbol{c} = \frac{\omega}{K}\mathbf{e}_K = \frac{\omega}{K^2}(k\mathbf{e}_x + m\mathbf{e}_z), \tag{2.44}$$

which is the velocity that any one frequency component of the wave (like a crest or a trough) travels at; and the group velocity ($\boldsymbol{c}_g$),

$$\boldsymbol{c}_g = \frac{\partial\omega}{\partial k}\mathbf{e}_x + \frac{\partial\omega}{\partial l}\mathbf{e}_y + \frac{\partial\omega}{\partial m}\mathbf{e}_z = \frac{Nm}{K^3}(m\mathbf{e}_x - k\mathbf{e}_z) \tag{2.45}$$

which is the velocity at which the overall wave envelope travels. It can also be thought of as the velocity at which energy or information is conveyed along a wave. The dot product of the phase and group velocity produces

$$\boldsymbol{c} \cdot \boldsymbol{c}_g = 0, \tag{2.46}$$

which shows us that *the phase and the group velocity vectors are perpendicular!* This is a counter intuitive relationship because this means that the wave and the energy carried by the wave are moving perpendicular to each other, which is unlike surface and interfacial waves.

What we have discussed so far is a linear treatment of internal gravity waves. The governing equations are nonlinear, and wave nonlinearity is quantified by the Froude number Fr, a ratio between the inertial and buoyancy effects

$$\mathrm{Fr} = \frac{U}{NL}, \tag{2.47}$$

where U is the typical oscillating velocity, and $L \equiv 1/|\boldsymbol{k}|$ is the wavelength.

2.3 Turbulence in geophysical flows

So far, we have we have described turbulence with assumptions of homogeneity, stationarity and isotropy as employed by Kolmogorov. However in geophysical turbulence, the symmetry of these assumptions is upset by rotation, stratification and shear effects. The largest scales in geophysical flows are dominated by the energy containing internal wave activity, and at the smallest scales the Kolmogorov isotropic turbulence is dominant. In between these two extremes, we have what is called the buoyancy-range or the saturation-range which is extremely anisotropic. A proposed theoretical model for the kinetic energy spectra in the buoyancy-range when N is assumed to be a constant is (Carnevale et al. [2001])

$$E(k) = \alpha N^2 k^{-3}. \tag{2.48}$$

Note that this spectrum depends only on the Brunt-Väisälä frequency N and the wavenumber k. The constant α is an empirical constant determined to be about 0.47. Since stratification affects only the vertical direction, we can assume horizontal isotropy. If we consider the kinetic energy spectra of the horizontal velocities (u, v) and vertical velocities w separately, then $\alpha \approx 0.2$ for the spectrum of either component (cf. Gargett et al. [1981]).

As we've already discussed in Section 2.1.3, the inertial-range kinetic spectra is given by

$$E(k) = C_K \varepsilon^{2/3} k^{-5/3}, \tag{2.22}$$

where ε is the turbulent dissipation rate, C_K is the empirical Kolmogorov constant which is determined to about 1.5. For the energy spectra of just one component of the velocity field, we would have to multiply C_K by 1/3 as the spectra is isotropic.

By matching the two kinds of spectra, we can estimate the Ozmidov wavenumber k_O where the buoyancy-range starts, up to an order one multiplicative constant as

$$k_O = \sqrt{\frac{N^3}{\varepsilon}}. \tag{2.49}$$

Using the relation for the Kolmogorov scale (2.13), we can estimate the inertial-range wavenumber, k_ν as (again, up to an order one multiplicative constant),

$$k_\nu = \nu^{-3/4} \varepsilon^{1/4}. \tag{2.50}$$

Hence the anisotropic buoyancy-range in the kinetic energy spectra can be thought of as existing between the wavenumbers k_O and k_ν, and the isotropic dissipation-range exists beyond the wavenumber k_ν.

Chapter 3

Numerical Method

In this chapter we will describe and motivate the numerical method used in our turbulence simulations. We have already established the model we will be using for the simulations as the Navier-Stokes equations under the Boussinesq approximation. We will now discuss the spectral method and also its application to the Navier-Stokes equations.

Due to the recent growth of computational power, there has been a lot of interest in the study of turbulence using numerical methods. Although fluid turbulence is a very complicated phenomenon, it is deterministic, and it is possible to simulate its evolution. The spatial and temporal derivative operators in the governing equations are evaluated using a suitable numerical scheme (spectral, finite-difference, finite-volume, or finite-element methods). Given the initial state and boundary conditions, one can calculate deterministically all the properties of the fluid flow at at certain time. If the spatial mesh is taken small enough to resolve the smallest features of the flow (i.e., at the Kolmogorov scale), the simulation is termed a direct numerical simulation (DNS). It is usually performed for moderate Reynolds numbers, because at very high Reynolds numbers, the spatial resolution needed is to high and the method is too expensive. As of now, computing clusters are available that enable us to run DNSs of up to 1000^3 resolution quite easily (DNS studies of 4096^3 (Kaneda et al. [2003]) and higher have been performed). For very high Reynolds numbers, a possible approach is utilizing a large-eddy simulation (LES), where the small scales are filtered out, but the large scales are evolved. For practical purposes, LESs are more useful because they allow us to determine the dynamics of coherent vortices and the statistical qualities of turbulence for a wide variety of high Reynold number flows. However, LESs contain some errors due to the inaccuracy of the numerical schemes and the incomplete resolution of the smallest scales.

3.1 The spectral method

3.1.1 Series-expansion methods

Series-expansion methods are a general class of numerical methods that encompass the spectral, pseudospectral and finite element methods. All three of these methods share a common foundation that we will discuss in this section. The discussion in this section follows Chapter 4 from Durran [1999].

Consider the simple partial differential equation

$$\frac{\partial \psi}{\partial t} + F(\psi) = 0 \tag{3.1}$$

with initial conditions $\psi(x, t_0) = f(x)$, and some boundary conditions specified at the edge of the spatial domain S. Here F is some operator involving spatial derivatives of ψ. A series-expansion method seeks to approximate the spatial dependence of ψ as a linear combination of a finite number of predetermined expansion functions, called *basis functions*. For a continuous function $\phi(x, t)$, we write the general form of the expansion as

$$\phi(x, t) = \sum_{k=1}^{N} a_k(t)\, \varphi(x), \tag{3.2}$$

where $\varphi_1, \cdots, \varphi_N$ are predetermined expansion functions satisfying the required boundary conditions of ψ on S. To solve (3.1) one only needs to determine the unknown coefficients $a_1(t), \cdots, a_N(t)$ so that the error in the solution is minimized. We quantify this requirement by defining the *residual*

$$R(\phi) = \frac{\partial \phi}{\partial t} + F(\phi), \tag{3.3}$$

which is the amount by which the approximate solution fails to satisfy the governing equation (3.1).

There are three broad strategies for minimizing the residual, and each leads to a system of coupled ordinary differential equations for the coefficients $a_1(t), \cdots, a_N(t)$. The first strategy is to minimize the square of the ℓ_2-norm of the residual

$$(\|R(\phi)\|_2)^2 = \int_S [R(\phi(x))]^2 \, \mathrm{d}x. \tag{3.4}$$

The second approach, called a *collocation* method, is to require the residual to be zero at a discrete set of grid points,

$$R(\phi(j\Delta x)) = 0, \qquad \text{for all } j = 1, \cdots, N. \tag{3.5}$$

The third strategy, known as the Galerkin approximation, requires that residual to be orthogonal to each of the expansion functions, i.e.,

$$\int_S R(\phi(x))\, \varphi_k(x)\, \mathrm{d}x = 0, \qquad \text{for all } k = 1, \cdots, N. \tag{3.6}$$

The collocation strategy is used in the pseudospectral method and some finite-element formulations. The spectral method uses the Galerkin formulation. Note that for the problem (3.1), the ℓ_2-norm minimization and Galerkin approximation are equivalent (refer [Durran, 1999, Section 4.1]).

3.1.2 The spectral method

Opting for the third strategy (3.6), we find that a system of ODEs are obtained for the unknown coefficients $a_1(t), \cdots, a_N(t)$,

$$0 = \int_S R(\phi)\varphi_k \,\mathrm{d}x = \int_S \left[\sum_{n=1}^{N} \dot{a}_n \varphi_n + F\left(\sum_{n=1}^{N} a_n \varphi_n\right)\right] \varphi_k \,\mathrm{d}x \quad \forall\, k = 1, \cdots, N.$$

or,

$$\sum_{n=1}^{N} I_{nk} \frac{\mathrm{d}a_n}{\mathrm{d}t} = -\int_S \left[F\left(\sum_{n=1}^{N} a_n \varphi_n\right) \varphi_k\right] \mathrm{d}x \quad \forall\, k = 1, \cdots, N, \tag{3.7}$$

where

$$I_{nk} = \int_S \varphi_n \varphi_k \,\mathrm{d}x. \tag{3.8}$$

The initial conditions for the system (3.7) are chosen so that $a_1(t_0), \cdots, a_N(t_0)$ and hence $\phi(x, t_0)$ provide the "best" approximation to $f(x)$. This is done in a similar fashion, by setting the Galerkin requirement that the initial error be orthogonal to each of the basis functions,

$$\int_S \left(\sum_{n=1}^{N} a_n(t_0)\varphi_n(x) - f(x)\right) \varphi_k(x) \,\mathrm{d}x = 0 \quad \forall\, k = 1, \cdots, N \tag{3.9}$$

or,

$$\sum_{n=1}^{N} I_{nk} a_n = \int_S f(x)\varphi_k(x)\,\mathrm{d}x \quad \forall\, k = 1, \cdots, N. \tag{3.10}$$

The defining characteristic of the spectral method is that **the basis functions form an orthogonal set**. This means that I_{nk} is zero unless $n = k$. Hence the system (3.7) reduces to

$$\frac{\mathrm{d}a_n}{\mathrm{d}t} = -\frac{1}{I_{kk}} \int_S \left[F\left(\sum_{n=1}^{N} a_n \varphi_n \right) \varphi_k \right] \mathrm{d}x \quad \forall\, k = 1, \cdots, N, \tag{3.11}$$

and the initial conditions (3.10) reduce to

$$a_k(t_0) = \frac{1}{I_{kk}} \int_S f(x)\varphi_k(x)\,\mathrm{d}x. \tag{3.12}$$

3.1.3 The Fourier-Galerkin spectral method

The geometry of the problem we are dealing with and periodic boundary conditions dictate that we use Fourier coefficients as the basis functions. We demonstrate the Fourier-Galerkin spectral method using a the simplest nonlinear partial differential equation, the Burgers equation. We also demonstrate the importance of *dealiasing*, and how dealiasing is performed using Orszag's transform method (cf. Orszag [1971]), commonly called the 2/3 rule.

Consider the Burgers equation in one dimension,

$$\frac{\partial u}{\partial t} + u\frac{\partial u}{\partial x} = \nu \frac{\partial^2 u}{\partial u^2} \tag{3.13}$$

whose solution we seek on a periodic domain $-\pi < x < \pi$, with initial condition $u(x, 0) = f(x)$. Multiply (3.13) by a test function $v \in H_0^1$ and integrate by parts on the nonlinear term to obtain the weak conservative form of the Burgers equation as

$$\int_{-\pi}^{\pi} \frac{\partial u}{\partial t}\, v \;\mathrm{d}x = \int_{-\pi}^{\pi} u^2 \frac{\partial v}{\partial x} - \nu \frac{\partial u}{\partial x}\frac{\partial v}{\partial x}\,\mathrm{d}x = 0, \quad \forall v \in H_0^1. \tag{3.14}$$

In the inner product notation $\langle f, g\rangle = \int_{-\pi}^{\pi} f(x)\,\overline{g(x)}\;\mathrm{d}x$, equation (3.14) can be written as

$$\langle \frac{\partial u}{\partial x}, v\rangle = \langle \frac{1}{2}u^2 - \nu \frac{\partial u}{\partial x}, \frac{\partial v}{\partial x}\rangle. \tag{3.15}$$

To apply the Fourier-Galerkin method, choose

$$u(x,t) = \sum_{k=-K+1}^{K} a_k(t)\, e^{i\,k\,x}. \tag{3.16}$$

where the Fourier coefficients a_k are $a_k(t) = \int_{-\pi}^{\pi} u(x,t)\, e^{-i\,k\,x}\, \mathrm{d}x$, and

$$v \in \mathrm{span}\{e^{i\,k\,x} : k = -K, \cdots, K\}. \tag{3.17}$$

Due to the orthogonality relation

$$\int_{\pi}^{\pi} e^{i\,n\,x}\, e^{-i\,m\,x}\, \mathrm{d}x = \begin{cases} 2\pi, & m = n \\ 0, & m \neq n. \end{cases}, \tag{3.18}$$

the terms of the equation (3.15) reduce to

$$\langle u_t, e^{i\,k\,x}\rangle = \langle \partial_t \sum_n a_n\, e^{i\,n\,x}, e^{i\,k\,x}\rangle = 2\pi\, \partial_t\, a_k \tag{3.19}$$

and

$$\begin{aligned} \langle \frac{1}{2}u^2 - \nu\, \frac{\partial u}{\partial x}, \partial_x e^{i\,k\,x}\rangle &= \langle (\sum_m a_m\, e^{i\,m\,x})(\sum_n a_n\, e^{i\,n\,x}) - \nu\, \partial_x \sum_m a_m\, e^{i\,m\,x}, i\,k\, e^{i\,k\,x}\rangle \\ &= \langle \frac{1}{2}\sum_m \sum_n a_m\, a_n\, e^{i\,(m+n)\,x}, i\,k\, e^{i\,k\,x}\rangle - \langle \nu\, i \sum_m m\, a_m e^{i\,m\,x}, i\,k\, e^{i\,k\,x}\rangle \\ &= -i\,\pi\,k \sum_{m+n=k} a_m\, a_n - 2\pi\,\nu\,k^2\, a_k. \end{aligned} \tag{3.20}$$

Thus the equation (3.15) breaks into a set of ODEs

$$\frac{\mathrm{d}a_k}{\mathrm{d}t} + \frac{i\,k}{2} \sum_{m=-K+1}^{K} a_m\, a_{k-m} + \nu\, k^2\, a_k = 0, \quad k = -K+1, \cdots, K. \tag{3.21}$$

The straightforward computation of the linear convolution sum

$$\sum_{m=-K+1}^{K} a_m\, a_{k-m}, \quad k = -K+1, \cdots, K \tag{3.22}$$

in the wave-number space takes $\mathcal{O}(K^2)$ operations. Since this is a unreasonable expense to bear at each time-step, Orszag (1970) proposed the transform method (cf. [Durran, 1999, Section 4.2.2]) which employs three Fast Fourier Transforms (FFT) to perform this operation in $\mathcal{O}(K \log K)$ operations.

The idea behind the transform method is to transform u to the physical space, and compute the product u^2, and transform it back to wave-number space. This operation is identical to computing the convolution sum as given by (3.22), provided there is enough spatial resolution to avoid aliasing error. Suppose that the physical space mesh is defined as

$$x_j = \frac{2\pi\, j}{2N}, j = 1, \cdots, 2N \tag{3.23}$$

and we consider the Fourier expansion of $u(x,t)$

$$u(x_j, t) = \sum_{k=-N+1}^{N} a_k(t)\, e^{i\,k\,x_j}, \tag{3.24}$$

where

$$a_l = 0, \text{ for } \quad K < |l| \leq N. \tag{3.25}$$

The question we want to answer is: what should be the physical resolution $2N$ so that there will be no aliasing?

Substitute the expansion of $u(x_j, t)$ into the kth component of the FFT (computed at the grid points (3.23)),

$$p_k = \frac{1}{2N} \sum_{j=1}^{2N} u(x_j, t)^2 e^{-i\,k\,x_j}, \tag{3.26}$$

to obtain

$$p_k = \sum_{m=-K+1}^{k} \sum_{n=-K+1}^{k} a_m\, a_n \left(\frac{1}{2N} \sum_{j=1}^{2N} e^{i\,(m+n-k)\,x_j} \right). \tag{3.27}$$

Due to the discrete version of the orthogonality relation (3.18), the above equation reduces to,

$$p_k = \sum_{m=-N+1}^{N} a_m\, a_{k-m} + \sum_{m=-N+1}^{N} a_m\, a_{k+2N-m} + \sum_{m=-N+1}^{N} a_m\, a_{k-2N-m}. \tag{3.28}$$

The second and third expressions in the above expansion represent the aliasing error, and only one of them will be non zero for a given value of k. For a negative value of k,

$$\sum_{m=-N+1}^{N} a_m \, a_{m+2N-k} \tag{3.29}$$

will tend to be non zero. If follows from (3.25) that $a_m \, a_{k-m} = 0$ if $m > K$, so all the terms in the above summation will be zero if $k + 2N > 2K$. In the most extreme case of $k = -K + 1$, the inequality is $N > (3K - 1)/2$. Hence a choice of $N = 3K/2$ is sufficient for dealised convolutions.

The procedure used to implement the transform method for the Burgers equation on a periodic one dimensional domain $-\pi < x < \pi$ is summarized by this algorithm:

- Truncate the Fourier coefficients a_k of u so that $a_k = 0$ for $2N/3 \leq k \leq N$.
- Perform the inverse FFT to obtain u in the physical space.
- Compute the product u^2 in the physical space.
- Perform the FFT of u^2, and truncate the Fourier coefficients at wavenumbers $k \geq 2N/3$.
- Step Fourier coefficients forward using a desired time stepping scheme.

A simple one-dimensional demonstration of the Fourier-Galerkin spectral method with dealiasing using Orszag's 2/3 rule is included in Appendix A.

3.2 Navier-Stokes equations in Fourier space

We will now formulate the Navier-Stokes in Fourier domain following the same method outlined in [Lesieur, 2008, Section 5.3]. Recall the Navier-Stokes equations (2.1-2.2),

$$\frac{\partial \boldsymbol{u}}{\partial t} + \boldsymbol{u} \cdot \nabla \boldsymbol{u} = -\frac{1}{\rho} \nabla p + \nu \nabla^2 \boldsymbol{u}, \tag{2.1}$$

$$\nabla \cdot \boldsymbol{u} = 0. \tag{2.2}$$

Consider a function $f(x, y, z, t)$, and its Fourier transform $\mathcal{F}(f) = \hat{f}(k_1, k_2, k_3, t)$. Then the Fourier transform of $\partial f/\partial x$ is $\mathrm{i}k_1\hat{f}(k_1, k_2, k_3, t)$. Hence, casting (2.2) into Fourier space gives us

$$\boldsymbol{k} \cdot \hat{\boldsymbol{u}}(\boldsymbol{k}, t) = 0, \tag{3.30}$$

which shows us that velocity $\hat{\boldsymbol{u}}(\boldsymbol{k}, t)$ is in a plane Π that is perpendicular to $\boldsymbol{k}$. Similarly, $\partial\hat{\boldsymbol{u}}(\boldsymbol{k}, t)/\partial t$ and $\nu k^2\hat{\boldsymbol{u}}$ are in the same plane Π. On the other hand, the pressure gradient $\mathrm{i}\hat{p}\boldsymbol{k}$ is parallel to $\boldsymbol{k}$.

Write the equation (2.1) in Fourier space

$$\frac{\partial\hat{\boldsymbol{u}}}{\partial t} + \mathcal{F}(\boldsymbol{u} \cdot \nabla\boldsymbol{u}) = -\frac{1}{\rho}\boldsymbol{k}\hat{p} - \nu k^2\hat{\boldsymbol{u}}, \tag{3.31}$$

and take dot product with $\boldsymbol{k}$ on either side, and use the orthogonality relation (3.30) to obtain

$$\boldsymbol{k} \cdot \mathcal{F}(\boldsymbol{u} \cdot \nabla\boldsymbol{u}) + \frac{1}{\rho}k^2\hat{p} = 0. \tag{3.32}$$

The above relation allows us to isolate the pressure term $\hat{p}$, and substitute it back into (3.31),

$$\frac{\partial\hat{\boldsymbol{u}}}{\partial t} + \mathcal{F}(\boldsymbol{u} \cdot \nabla\boldsymbol{u})(\mathbf{1} - \frac{\boldsymbol{k}\boldsymbol{k}}{k^2}) = -\nu k^2\hat{\boldsymbol{u}}. \tag{3.33}$$

Here, we note that the term $\mathbf{1} - \boldsymbol{k}\boldsymbol{k}/k^2$ that multiplies the Fourier transform of the advection term. The rest of the terms are in a plane parallel to $\hat{\boldsymbol{u}}$. Hence, we can imagine $\mathbf{1} - \boldsymbol{k}\boldsymbol{k}/k^2$ as being a projection operator into the $\hat{\boldsymbol{u}}$-plane. Hence, we are getting rid of the pressure term by projecting the advection term onto the $\hat{\boldsymbol{u}}$-plane.

We call

$$\boldsymbol{P} = \mathbf{1} - \frac{\boldsymbol{k}\boldsymbol{k}}{k^2} \tag{3.34}$$

the projection tensor, which will project the Navier-Stokes onto the $\hat{\boldsymbol{u}}$-plane. In Einstein's summation notation it is written as

$$P_{ij}(\boldsymbol{k}) = \delta_{ij} - \frac{k_i k_j}{k^2}. \tag{3.35}$$

It is easy to verify that $P_{ij}P_{jk} = P_{ik}$, meaning that $\boldsymbol{P}$ is idempotent, $\boldsymbol{P}^2 = \boldsymbol{P}$. Also, by noting that $k_j P_{ij} = 0$ and $\hat{u}_j P_{ij} = \hat{u}_i$, we can verify that the projection tensor projects a vector to the $\hat{\boldsymbol{u}}$-plane.

Apply $\boldsymbol{P}$ to (3.31) to obtain

$$\frac{\partial \hat{\boldsymbol{u}}}{\partial t} + \boldsymbol{P}\mathcal{F}(\boldsymbol{u} \cdot \nabla \boldsymbol{u}) = -\nu k^2 \hat{\boldsymbol{u}}. \tag{3.36}$$

The term $\mathcal{F}(\boldsymbol{u} \cdot \nabla \boldsymbol{u})$ still needs to be calculated. To do so, rewrite

$$\boldsymbol{u} \cdot \nabla \boldsymbol{u} = u_j \frac{\partial u_i}{\partial x_i} = \frac{\partial (u_i u_j)}{\partial x_j} \tag{3.37}$$

using the incompressibility condition (2.2). By the convolution product property of the Fourier transform, we write

$$\mathcal{F}(\boldsymbol{u} \cdot \nabla \boldsymbol{u}) = \mathrm{i}k_j \mathcal{F}(u_i u_j) = \mathrm{i}k_j \int_{\boldsymbol{p}+\boldsymbol{q}=\boldsymbol{k}} \hat{u}_i(\boldsymbol{p}, t)\hat{u}_j(\boldsymbol{p}, t)\, \mathrm{d}\boldsymbol{p}. \tag{3.38}$$

Putting everything together, the Navier-Stokes equations in Fourier space are

$$\frac{\partial u_i}{\partial t} + \mathrm{i}P_{ij}(\boldsymbol{k})k_m \int_{\boldsymbol{p}+\boldsymbol{q}=\boldsymbol{k}} \hat{u}_j(\boldsymbol{p}, t)\hat{u}_m(\boldsymbol{q}, t)\, \mathrm{d}\boldsymbol{p} = -\nu k^2 \hat{u}_i, \tag{3.39}$$

$$\boldsymbol{k} \cdot \hat{\boldsymbol{u}}(\boldsymbol{k}, t) = 0. \tag{3.30}$$

For the numerical formulation, the direct evaluation in Fourier space of the convolution product in (3.39) is not very convenient for implementation. Hence, we will rewrite the advection term in a form that is suitable for numerical evaluation. Starting from the identity

$$\boldsymbol{u} \cdot \nabla \boldsymbol{u} = \boldsymbol{\omega} \times \boldsymbol{u} - \frac{1}{2}\nabla u^2, \tag{3.40}$$

and applying the projection operator $\boldsymbol{P}$, we notice that the ∇u^2 vanishes because it is orthogonal to the $\hat{\boldsymbol{u}}$-plane. For the Fourier transform of the advection term, we use the transform method discussed in Section 3.1.3,

$$\mathcal{F}(\boldsymbol{\omega} \times \boldsymbol{u}) = \mathcal{F}(\mathcal{F}^{-1}(\hat{\boldsymbol{\omega}}) \times \mathcal{F}^{-1}(\hat{\boldsymbol{u}})). \tag{3.41}$$

For direct numerical simulations of turbulence, the preferred form of the Navier-Stokes equations in Fourier space is (refer Orszag and Patterson Jr [1972]).

$$\frac{\partial \hat{\boldsymbol{u}}}{\partial t} + \boldsymbol{P}(\boldsymbol{k})\mathcal{F}(\mathcal{F}^{-1}(\hat{\boldsymbol{\omega}}) \times \mathcal{F}^{-1}(\hat{\boldsymbol{u}})) = -\nu k^2 \hat{\boldsymbol{u}}. \tag{3.42}$$

This formulation has the same advantages as (3.39) because of the absence of the pressure term. The pressure can still be evaluated whenever it is needed using (3.32). The Boussinesq equations can be written in Fourier space using a similar method (cf. Lesieur [2008]).

3.2.1 Note on the timestepping method

The equation (3.42) are actually a coupled system of ordinary differential equations. Each Fourier mode has an equation of the form

$$\frac{\mathrm{d}\psi}{\mathrm{d}t} + r\psi = F(\psi). \tag{3.43}$$

Using an integrating factor, the left hand side of (3.43) can be written as

$$\frac{\mathrm{d}\psi}{\mathrm{d}t} + r\psi = \mathrm{e}^{-rt}\frac{\mathrm{d}(\psi\,\mathrm{e}^{-rt})}{\mathrm{d}t}. \tag{3.44}$$

Hence we have

$$\frac{\mathrm{d}(\psi\,\mathrm{e}^{-rt})}{\mathrm{d}t} = F(\psi)\,\mathrm{e}^{rt}, \tag{3.45}$$

which we can solve using many different timestepping methods (cf. [Durran, 1999, Section 2.3]). We use a third-order Adams-Bashforth scheme,

$$\psi^{n+1}\,\mathrm{e}^{r(t_n+\Delta t)} - \psi^n\,\mathrm{e}^{rt_n} = \frac{23}{12}\Delta t\,\mathrm{e}^{rt_n}F(\psi^n) - \frac{4}{3}\Delta t\,\mathrm{e}^{rt_{n-1}}F(\psi^{n-1}) + \frac{5}{12}\Delta t\,\mathrm{e}^{rt_{n-2}}F(\psi^{n-2}), \tag{3.46}$$

or,

$$\psi^{n+1} = \mathrm{e}^{-\Delta t}\psi^n + \frac{23}{12}\Delta t\,\mathrm{e}^{-\Delta t}F(\psi^n) - \frac{4}{32}\Delta t\,\mathrm{e}^{-2\Delta t}F(\psi^{n-1}) + \frac{5}{12}\Delta t\,\mathrm{e}^{-3\Delta t}F(\psi^{n-2}). \tag{3.47}$$

3.2.2 Note on the code

The code used for running the simulations in report was developed by Michael Waite based on an earlier version by Peter Bartello, and it has a proven track record for stratified turbulence simulations (eg. Waite and Bartello [2004], Waite [2011]). The code, written in Fortran 90, uses the spectral method discussed in Section 3.1 to perform a DNS of the Navier-Stokes equations under the Boussinesq approximation, (2.23-2.25) in a periodic domain of the size $L_1 \times L_2 \times L_3$ discretized into $M_1 \times M_2 \times M_3$ points. The code is parallelized along the z axis using Open MPI v1.6, so each processor only has to deal with one slice of the cubic domain. For switching between the Fourier and physical domains, the code uses FFTW v3.3 (Frigo and Johnson [2005]). For computing the dealiased nonlinear terms, the transform method discussed in Section 3.1 is used. Hence the Fourier coefficients along all directions are truncated at two thirds the maximum wavenumber, $M_i/3$. The timestepping method used is the third order Adams-Bashforth scheme that was just discussed. The code also uses the NetCDF library for periodic data dumps of the real space fields. It also dumps restart files (which are the Fourier space fields $(\boldsymbol{\omega}, \rho')$ being solved for) at the end of a simulation which can be used to resume the simulation from the same point in time.

Some modifications to the code had to be performed to adapt for a high resolution 1024^3 DNS. Originally, the Fourier fields being dumped at the end of the simulation were stored in a single file. However, the NetCDF library has a constraint of being able to support only one very large variable in a single file. So the code had to be modified to put the four fields $(\boldsymbol{\omega}, \rho')$ in four different files. Also, originally the code used FFTW2, which is now considered obsolete and has not been upgraded since 1999. FFTW3 is faster and supports three-dimensional inplace distributed memory transforms without using MPI function calls, but is not backward compatible with FFTW2. Considerable effort was put into upgrading the code to FFTW3 to make use of these advantages.

Chapter 4

Problem

The original paper that motivated this project is Benielli and Sommeria [1996]. This is an experimental study where the authors induce standing internal gravity waves in a cubic tank with salt solution that is linearly and stably stratified by varying the salinity. The tank is then vigorously oscillated in the vertical plane so that the apparent gravity is modulated around its mean value with some excitation frequency f_e. As discussed in Section 2.2.3, internal gravity waves can oscillate in any mode with frequency between 0 and the Brunt-Väsälä frequency N. In this case, a primary wave with the mode close to $f_e/2$ was observed to be amplified, $f_e/2$ being the frequency of the energy input. The growth of this primary wave is quickly curtailed by nonlinear effects; an instability occurs, and the wave overturns leading rapidly to turbulence.

During the experiment, the authors measure the salinity (and hence the density) at the center of the tank using a conductivity probe. The power spectrum of the time series of this data exhibits a peak at frequency $f_e/2$ as expected. At higher frequencies, beyond $N/2\pi$ where internal wave activity ends and the buoyancy-range begins, a f^{-3} spectrum is clearly observed in over two decades on the logarithmic scale.

When making measurements at a single point, it is often assumed that the turbulence is "frozen". This is known as *Taylor's frozen turbulence hypothesis* (Taylor [1938]), which assumes that the advection velocity of the turbulence is much greater than the velocity scale of the turbulence itself. Mathematically, this means that for any fluid property ζ, its material derivative is zero, i.e., $\mathrm{d}\zeta/\,\mathrm{d}t = 0$. In other words the rate of change of ζ is only due to advection,

$$\frac{\partial \zeta}{\partial t} = -u\frac{\partial \zeta}{\partial x} - v\frac{\partial \zeta}{\partial y} - w\frac{\partial \zeta}{\partial z}. \tag{4.1}$$

Suppose that the mean advection velocity is U, then the time taken for eddies of size l to pass through the point of measurement is $t = l/U$, and corresponding measure frequency is $f = 2\pi/t$. This frequency f and the eddy wavenumber $k = 2\pi/l$ are hence related by $f = kU$.

In Benielli and Sommeria [1996] also, the authors invoke Taylor's hypothesis to relate the spatial wavenumber and the temporal frequency spectra, and conclude the presence of a k^{-3} density spectra. This kind of a spectrum is commonly observed in the buoyancy subrange of the oceans and atmosphere. In general, there is no simple relationship between the wavenumber and frequency spectra, and Taylor's hypothesis is usually held to be valid in situations such as wind tunnels, where the turbulence blows past the measurement point very quickly. But for turbulence in stratified fluids, the validity of Taylor's hypothesis is questionable. This is because the background advection velocity is due a standing wave, and it is not necessarily much larger than the turbulence velocity. One of the goals of this report is to verify the equivalence of the wavenumber and frequency spectra in a stratified medium using direct numerical simulations in which, unlike the experiment described above, the frequency and wavenumber spectra can be measured independently.

Two numerical studies that are directly related to the experiment that was just described are Bouruet-Aubertot et al. [1995] and Bouruet-Aubertot et al. [1996]. Both studies are two-dimensional direct numerical computations, and of fairly low resolution (either 128^2 or 256^2). In these simulations the numerical domain is square of side π, and the Brunt-Väsälä frequency is set to unity. The viscosity is set to its minimum possible value for a given spatial resolution so that all scales are well resolved. The the initial condition is a standing wave with a small amplitude, and the nonlinear evolution of this wave is observed until it breaks. It is found that the life time of the coherent wave is inversely proportional to the square of the amplitude. Also, it is observed that the wave breaking eventually occurs, whatever the wave amplitude. The authors also propose a mechanism for wave breaking and the transfer of energy from higher lower wavenumbers to higher wavenumbers, which involves resonant interactions of the parametric subharmonic instability type. The authors also observe the turbulent buoyancy subrange with the k^{-3} energy spectra during the decay after wave breaking.

Another related numerical study is Carnevale et al. [2001], where the authors examine the transition from the buoyancy-range to the inertial-range in stratified turbulence. The authors use a three dimensional large eddy simulation to examine the breaking of a standing wave in a 128^3 computational cube containing a stratified medium. Unlike the previous numerical studies where the wave was allowed to decay, the authors use forcing to maintain the amplitude. However the forcing wave has a small enough amplitude so that the primary wave is not overturned within one forcing cycle. A smaller amplitude allows wave-wave

interactions to produce smaller waves without being subject to shear instability. The authors observe the breaking of the wave and the transition from the anisotropic k^{-3} buoyancy-range spectra to the isotropic $k^{-5/3}$ inertial-range spectrum.

A review paper that examines the mechanisms associated with steepening and breaking of internal gravity waves in a stratified medium is Staquet and Sommeria [2002].

4.1 Set-up of the simulation

Our simulations are performed in a cube of dimensions $L_1 = L_2 = L_3 = 2\pi$ discretized at the resolution $M_1 = M_2 = M_3 = 1024$. Since we use the 2/3 rule for dealiasing, the number of wavenumbers retained in each direction is 341. The Brunt-Väisälä frequency given by (2.28), is taken to be $N = 1$, by setting the background density gradient $\mathrm{d}\bar{\rho}/\,\mathrm{d}z = -1$ and $g/\rho_0 = 1$. Also the molecular diffusivity is taken to be the same as the kinematic viscosity, $\kappa = \nu$.

Note that the difference between the densities at the bottom and top of the domains is 2π, and even though $\rho'/\rho_0 \ll 1$ is not true in this case, the Boussinesq approximation is still valid in our simulation. This is because when N is assumed to be a constant, ρ_0 does not appear independently in the equations (2.23-2.25) – one can verify this fact by making a change of variable, $b = -g\rho'/\rho_0$. There will be different combinations of g, ρ_0 and $\mathrm{d}\bar{\rho}/\,\mathrm{d}z$ that give the same constant N, but all that matters is the value of N.

The goal of this study is to observe the evolution of a simple standing wave in a stratified medium until breaking occurs. One way to do this by initialing the density field and keeping the velocity fields zero. Hence the system will begin in a state of maximum potential energy when oscillations start. As the initial condition, we initialize the perturbation density ρ',

$$\frac{\rho'}{\rho_0} = a\cos x\cos z, \tag{4.2}$$

$$(u, v, w) = (0, 0, 0). \tag{4.3}$$

with the amplitude set to $a = 1$. As noted by Bouruet-Aubertot et al. [1995], the amplitude affects the lifetime of the coherent wave (or the time required for breaking) and we expect faster breaking for larger amplitudes.

A linear solution of the system for the standing wave (4.2) is

$$\rho'(x,z,t) = a\rho_0 \cos x \cos z \cos \omega t \tag{4.4}$$

$$u(x,z,t) = -\frac{ag\omega}{N^2} \sin x \sin z \sin \omega t \tag{4.5}$$

$$w(x,z,t) = -\frac{ag\omega}{N^2} \cos x \cos z \sin \omega t, \tag{4.6}$$

with the frequency of the wave given by (2.43) as

$$\omega = \frac{N}{\sqrt{2}} = \frac{1}{\sqrt{2}} \tag{4.7}$$

and hence the time period as

$$T_L = \sqrt{2}\frac{2\pi}{N} = 2\pi\sqrt{2}. \tag{4.8}$$

This standing wave can be seen as a superposition of four pairs of travelling waves with frequencies, $\pm\omega$ and with wavenumber vectors $(1,0,1)$, $(-1,0,1)$, $(1,0,-1)$ and $(-1,0,-1)$. Hence, it is necessary to remember that the modes will not change by reversing any of the wavenumber components across (4.4-4.6), and the oscillation frequency is unchanged by reversing the sign of ω.

Note that the choices of size of the cube and N set the length and time scales respectively, and any general physical situation can be represented by setting these values. Before running the simulation, the kinematic viscosity is adjusted to get its minimum possible value so that the smallest spatial scales are well resolved. This is done by looking at the maximum value $\varepsilon_{\max}$ of the dissipation rate ε during the simulation, and making sure that the inertial-range wavenumber $k_\nu = \nu^{-3/4}\varepsilon_{\max}^{1/4}$ is less than the largest wavenumber that is resolved in our numerical method, which is 341. Another general rule of thumb is to make sure that at all times during the simulation, there is a well defined dissipation range in the kinetic energy spectra, where the energy drops to a very small value for large wavenumbers. After some experimentation, the value of kinematic viscosity is set to be $\nu = 10^{-4}$.

The initial condition (4.2), and hence the linear solution (4.4-4.6) is two-dimensional. Although this standing wave will eventually become unstable and generate turbulence, the turbulence will be constrained since there is no source of y-variation in the flow. To break this two-dimensional symmetry, we add a random initial perturbation of the order $a/100$ to the density field.

The evolution of the initial condition (4.2) involves nonlinear interactions, and hence the exact solution will be quite different from the linear solution. In fact, the two depart from each other progressively, and the importance of the nonlinear interactions can be estimated by the Froude number (2.47) as mentioned earlier. In our case,

$$\mathrm{Fr} = \frac{ag\omega}{N^3} \propto \frac{a}{N^2} \approx 1. \tag{4.9}$$

Also note that the Reynolds number (2.3) is of the order

$$\mathrm{Re} = \frac{(ag/2\omega)L}{\nu} = \frac{2\pi\sqrt{2}}{2 \cdot 10^{-4}} \approx 4 \times 10^4. \tag{4.10}$$

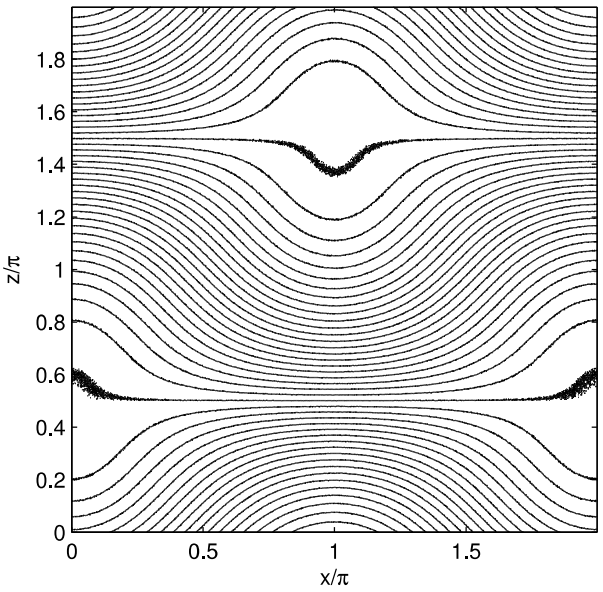

Figure 4.1: A contour plot of the initial density field $\rho = \rho' + \bar{\rho}$ given by (4.2) for a vertical x,z slice of the computational domain through $y = 0$. Each side of the domain is 2π units. Random noise of the order $a/100$ has been added throughout. The contour spacing is 0.1358.

The initial density perturbation has no variation along the y direction, and a representation of it on the plane $y = 0$ is shown in Figure 4.1. Note that this profile has two nodal planes at $z = \pi/2$ and $z = 3\pi/2$. The fluid above and below these planes approaches and retreats from them depending on the z coordinate. On the nodal plane $z = 3\pi/2$ at $x = 0, 2\pi$, and on the nodal plane $z = \pi/2$ at $x = \pi$, there are regions of 'compression' or centers of high oscillating strain. Similarly, on the nodal plane $z = \pi/2$ at $x = 0, 2\pi$, and on the nodal plane $z = 3\pi/2$ at $x = \pi$, there are regions of vertical 'dilation'.

4.2 Density field structures

The simulation was run for a long time (ten linear periods, $10T_L$), and we now will make some comments and observations about the evolution of the density field. From the time $t = 0$ to $t = 1.0T_L$, the linear approximation is a very indicator of how the density field is evolving. The effect of the nonlinearities is not yet pronounced. In Figure 4.2, we see that over one period, the region of vertical compression, which is originally around $(x, z) = (\pi, \pi/2)$ moves up to where the region of vertical dilation is around $(x, z) = (\pi, 3\pi/2)$, and returns to its original position. The random noise that is visible along lines of constant density at $t = 0$ smooths out, and they are no longer visible in subsequent times.

Further, we also observe that between $t = 0$ and $t = 3.0T_L$, even though the evolution progressively departs from the linear approximation, it is essentially two dimensional. We see in Figure 4.3, that for the first three periods the dissipation rate is only due to the evolution of the standing wave only. The breaking event itself occurs around $t = 3.65T_L$, when the dissipation blows up. Subsequently, the evolution of dissipation rate shows large fluctuations, although there is still a cyclical component corresponding to the initial standing wave.

Figure 4.6 captures the breaking event, the frames are ordered temporally (a) through (h); (a) corresponds to $3.0T_L$ and the interval between consecutive frames is $T_L/7$. Hence, (a) and (h) are in the same phase of oscillations. In (a), we can see that by $3.0T_L$, the density field has already departed quite a lot from the the initial condition of a standing wave. In (c) we can see the fold starting to form in the isodensity lines and the field is already unstable, and by (f) which is around $t = 3.71T_L$, the breaking seems to have started along with a lot of mixing happening between the layers. The folding is symmetric, and it is most pronounced around the regions of 'compression' that was discussed when describing the initial conditions. During the breaking event (f), we see that heavier fluid spills over lighter fluid, starting the mixing process between layers and leading to the creation of small-scale structures along the breaking region. Comparing (h) with (a), we see that the density field has become irreversibly unstable. An examination of the x and z slices of the density field shows that at this point the field is still two dimensional. The breaking of the wave begins the process of generation of three-dimensional turbulence.

If we further observe the evolution of the density field, we see that the wave will break again, but after about two and a half linear periods, at around $t = 6.0T_L$. By then, the flow is completely asymmetric and three-dimensional. This is observed in Figure 4.7, which are snapshots of the density field on the planes $x = 0$ and $y = 0$ between the times $5.5T_L$ and $6.5T_L$. This is also the point at which the dissipation rate is at a maximum and

the Kolmogorov dissipative scale η is at a minimum, as seen in Figures 4.3 and 4.4. The minimum value of the Kolmogorov dissipative scale is $\eta_{\min} = 0.0052$ which is within the smallest feature that is resolved in the simulation, $2\pi/1024 \simeq 0.0061$. Hence, this is a valid direct numerical simulation.

4.3 Energy spectrum

We now consider the total kinetic energy (KE) spectra of the flow at the same times as those in Figure 4.6. Just like Benielli and Sommeria [1996], we consider the spatial spectra in the vertical direction. Since the flow is not isotropic, we choose not to use the isotropic total wavenumber spectra. Along with the spectra, the lines representing the inertial-range spectrum $C_K\varepsilon^{2/3}k^{-5/3}$ and buoyancy-range spectrum $\alpha N^2 k^{-3}$ (refer Section 2.3) are also drawn. The ε is taken as the dissipation rate at that time, and the constants C_K and α are taken to be 1.5 and 0.2 respectively.

For Figure 4.8, which represents the vertical KE spectra during first breaking event, we see that the inertial-range is very shallow, and the potential and kinetic energy spectra drop off very quickly into the dissipation-range. At this point, the turbulence is not well developed and the flow is still two dimensional. But for the smaller wavenumbers (up to 20), we see a reasonable agreement with the k^{-3} buoyancy-range spectrum.

Figure 4.9 represents the vertical KE spectra during the secondary breaking event, when three-dimensional turbulence is fully developed, and the Kolmogorov dissipation scale η is the smallest. The estimated Ozmidov and inertial-range wavenumbers are $k_O \approx 20$ and $k_\nu \approx 180$ (the typical value of ε at this point in time being 10^{-3}). Indeed, between the wavenumbers of 20 and 180, we see very good agreement of the spectra with the $k^{-5/3}$ inertial-range spectrum.

We now consider the vertical KE spectra between the first and second wave breaking events in Figure 4.10. The first frame in the plot corresponds to the time $4.0T_L$, and the interval between consecutive frames is $T_L/7$. The dominant mechanism in this point of time is neither the large scale internal wave activity nor the small scale turbulent dissipation, but it is transport of fine-scale density structures by wave motion. Hence we should expect a wide buoyancy-range, and as expected this is seen in Figure 4.10. The spectra clearly aligns with the steeper k^{-3} line between the wavenumbers 10 to 80. We now turn our attention to the perturbation density at the center of the computational domain. In Figure 4.11, we have the physical values of the perturbation density ρ' at (π, π, π), the center of the computational domain, and underneath we have the power spectra of the signal through a

Hamming window vs the frequency. The point represented by the * is the $N/2\pi$ frequency which is the end of the internal wave domain in the frequency spectra. Beyond that point, for about one and half decades, there is a good fit with the f^{-3} power law. This verifies the assumption made in Benielli and Sommeria [1996] to use the Taylor's hypothesis to relate the wavenumber energy spectra with the frequency density spectra.

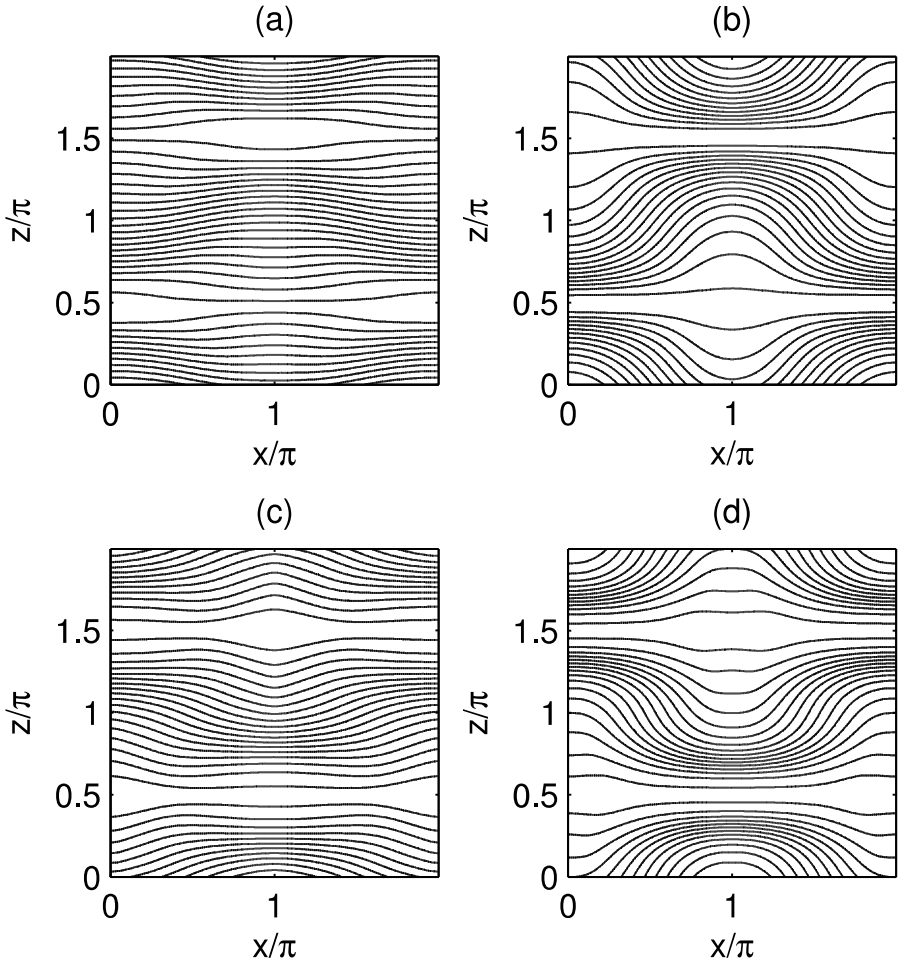

Figure 4.2: Nonlinear evolution of the total density fields after (a) one quarter (b) one half (c) three quarters and (d) one linear wave period T_L, with the initial conditions (4.2). Compare (d) with Figure 4.1 to estimate the importance of nonlinear effects after one linear period.

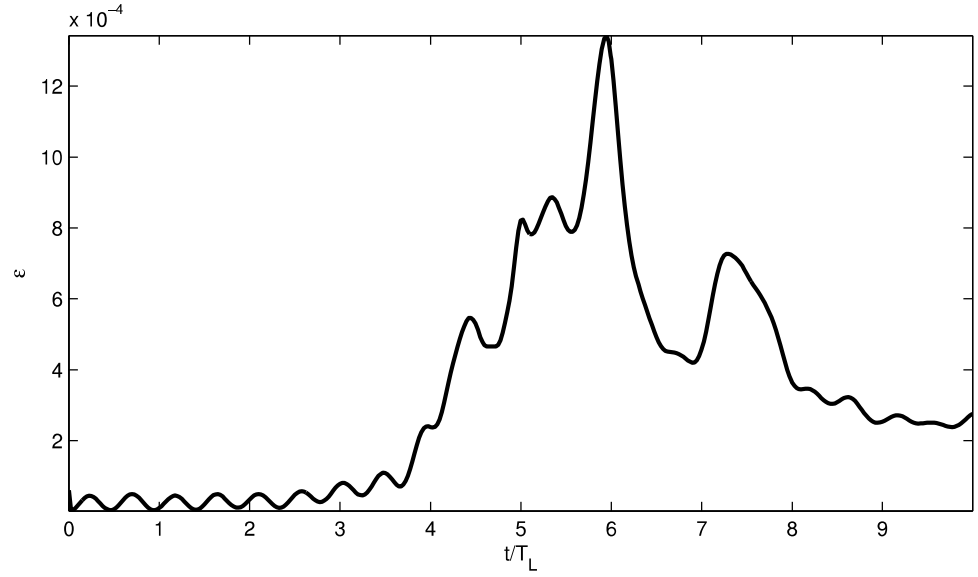

Figure 4.3: Plot of the total dissipation rate ε vs. the time in number of number of linear periods t/t_L, where $T_L = \sqrt{2}(2\pi)/N$. The blowup in ε starts at around $t = 3.65T_L$ and the maximum occurs at around $t = 5.95T_L$.

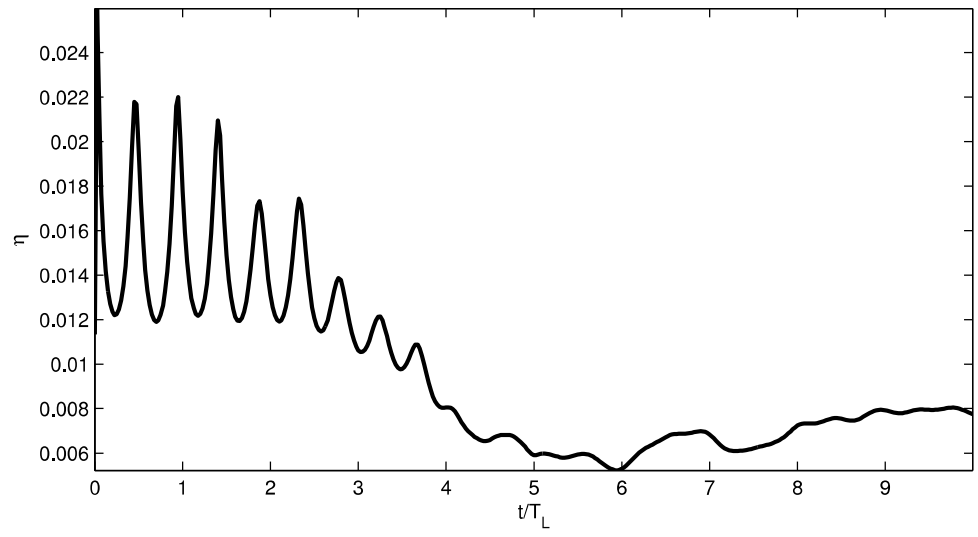

Figure 4.4: Plot of the Kolmogorov scale $\eta = (\nu^3/\epsilon)^{1/4}$ vs the time in number of linear periods t/T_L. The smallest Kolmogorov scales corresponds to the time at which we have highest dissipation rate.

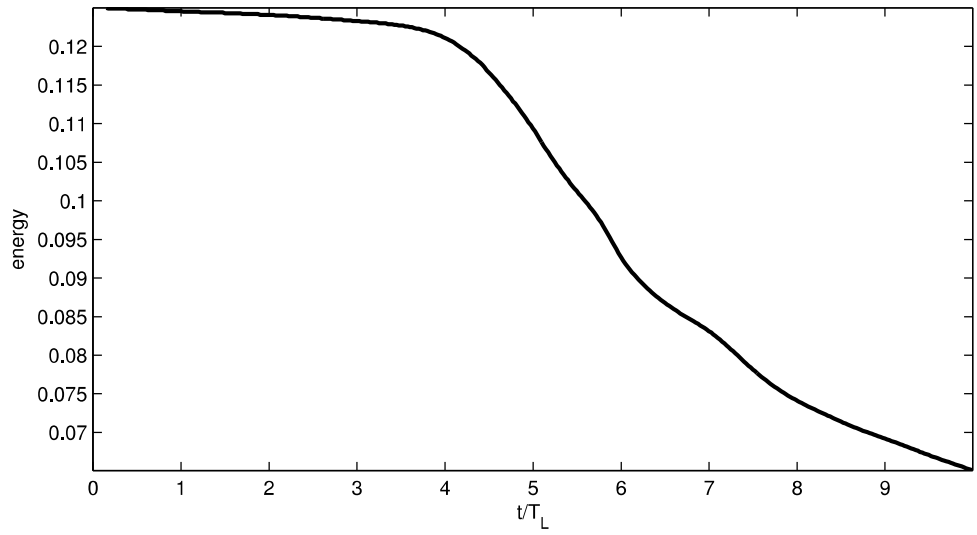

Figure 4.5: Plot of the total (kinetic + available potential) energy vs. the time in number of linear periods. At the around the same time the blowup in ε starts, there is a sharp decline in the total energy.

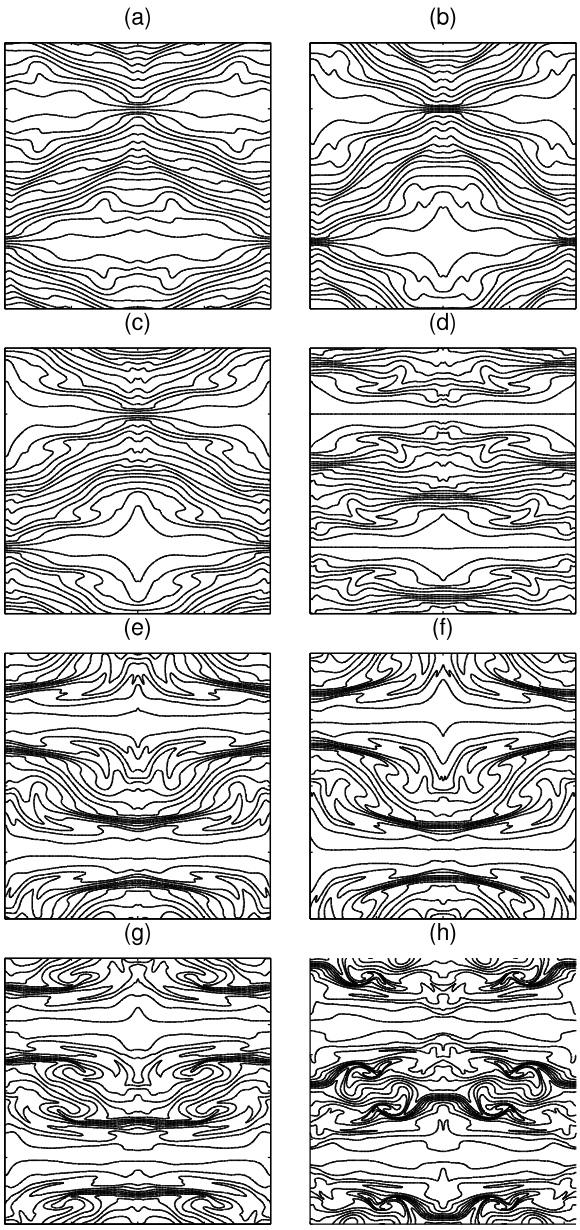

Figure 4.6: Total density field snapshots of the $y = 0$ plane during breaking. The frames are ordered by time from (a) to (h). The first one corresponds to $3.0T_L$ and the last one corresponds to $4.0T_L$. So the interval between snapshots is $T_L/7$. Unlike the secondary wave breaking event represented in Figure 4.7, we do not include the $x = 0$ slices because at this point the flow is still predominantly two-dimensional.

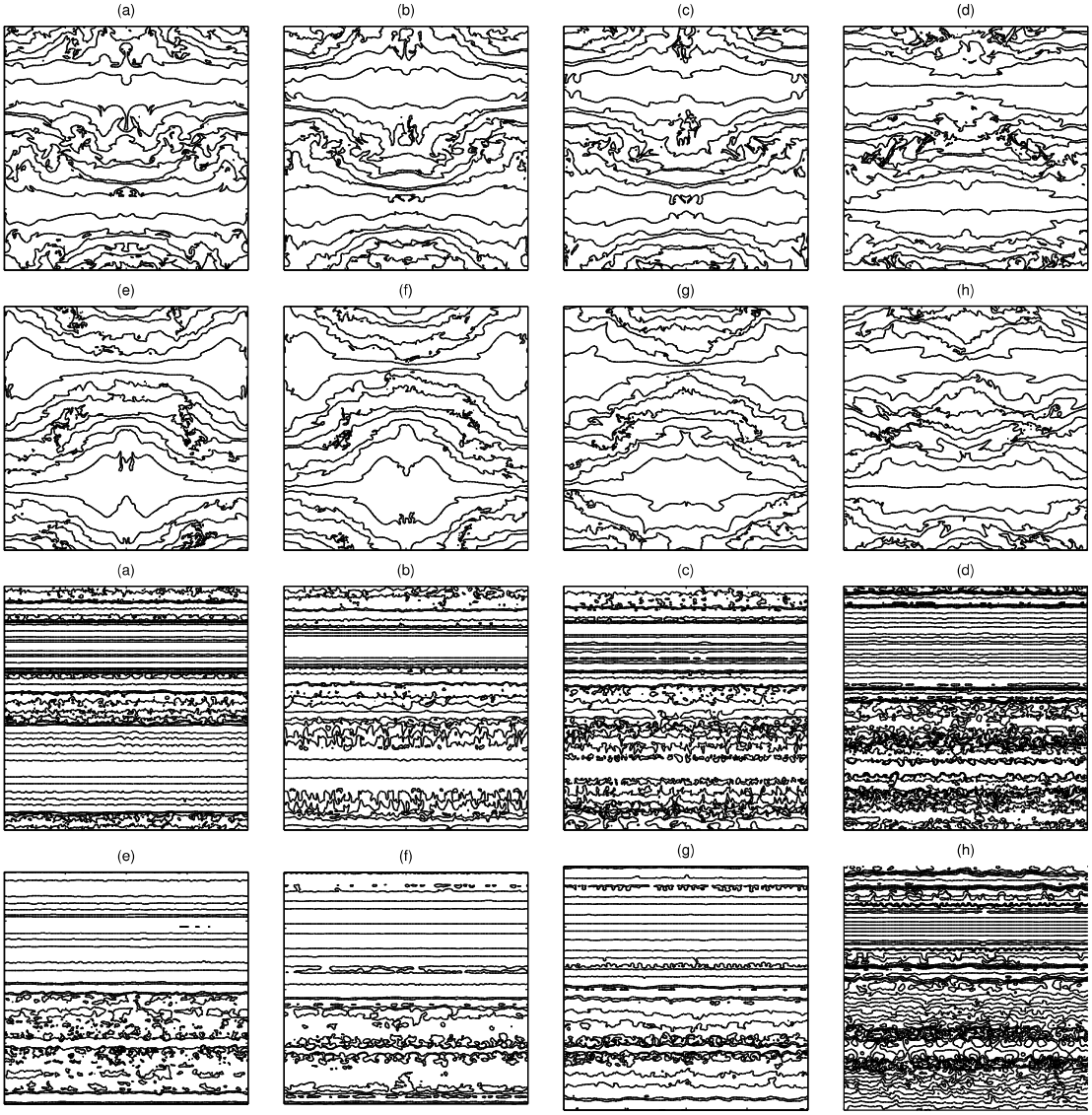

Figure 4.7: The top 8 panels are of the $y = 0$ plane, and the bottom 8 are the $x = 0$ plane during the secondary break. Panel (a) is at $5.5T_L$, and consecutive panels are $T_L/7$ apart. Originally, the $x = 0$ plane only contains straight lines, but after the secondary break we see a lot of small scale features develop.

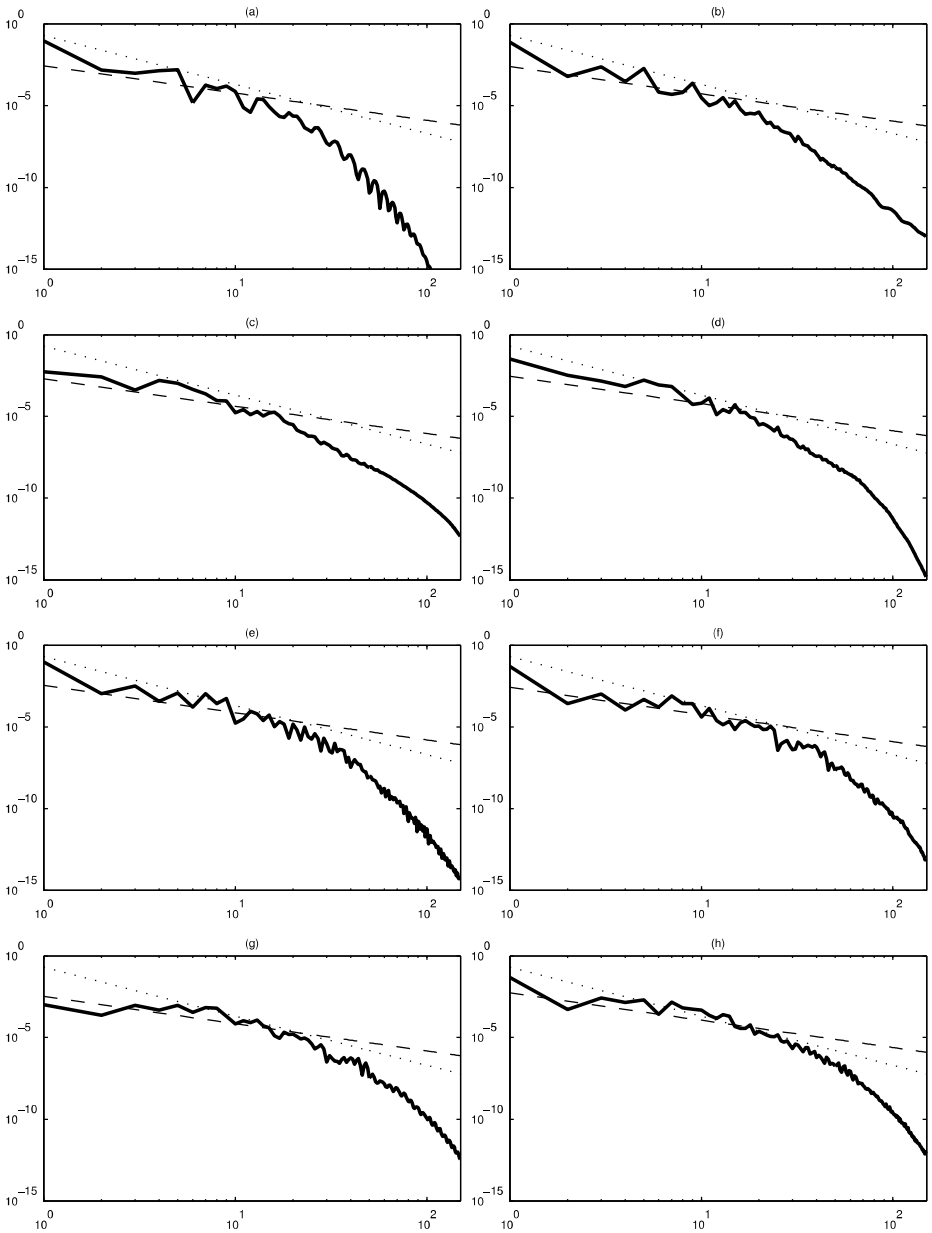

Figure 4.8: Kinetic energy spectra in the vertical direction for one linear timeperiod, corresponding to the density panels shown in Figure 4.6. First panel corresponds to $3.0T_L$, and the interval between consecutive panels is $T_L/7$. The dashed line represents the $(1/3)C_K\varepsilon^{2/3}k^{-5/3}$ inertial-range spectrum with $C_K = 1.5$ and the dotted line represents the $0.2N^2k^{-3}$ buoyancy-range spectrum.

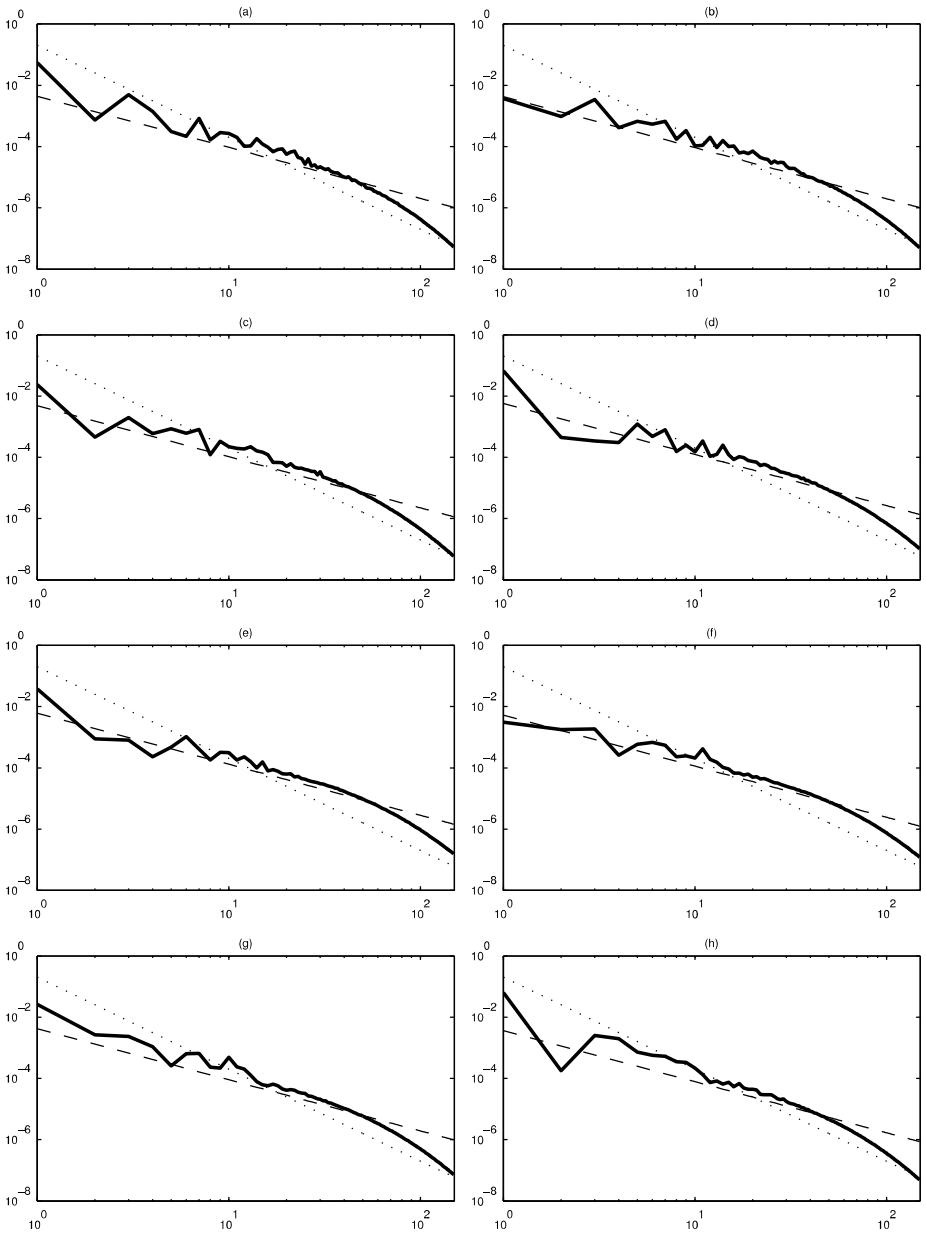

Figure 4.9: Kinetic energy spectra in the vertical direction for one linear timeperiod, corresponding to the density panels shown in Figure 4.7. First panel corresponds to $5.5T_L$, and the interval between consecutive panels is $T_L/7$. The dashed line represents the $(1/3)C_K\varepsilon^{2/3}k^{-5/3}$ inertial-range spectrum with $C_K = 1.5$ and the dotted line represents the $0.2N^2k^{-3}$ buoyancy-range spectrum.

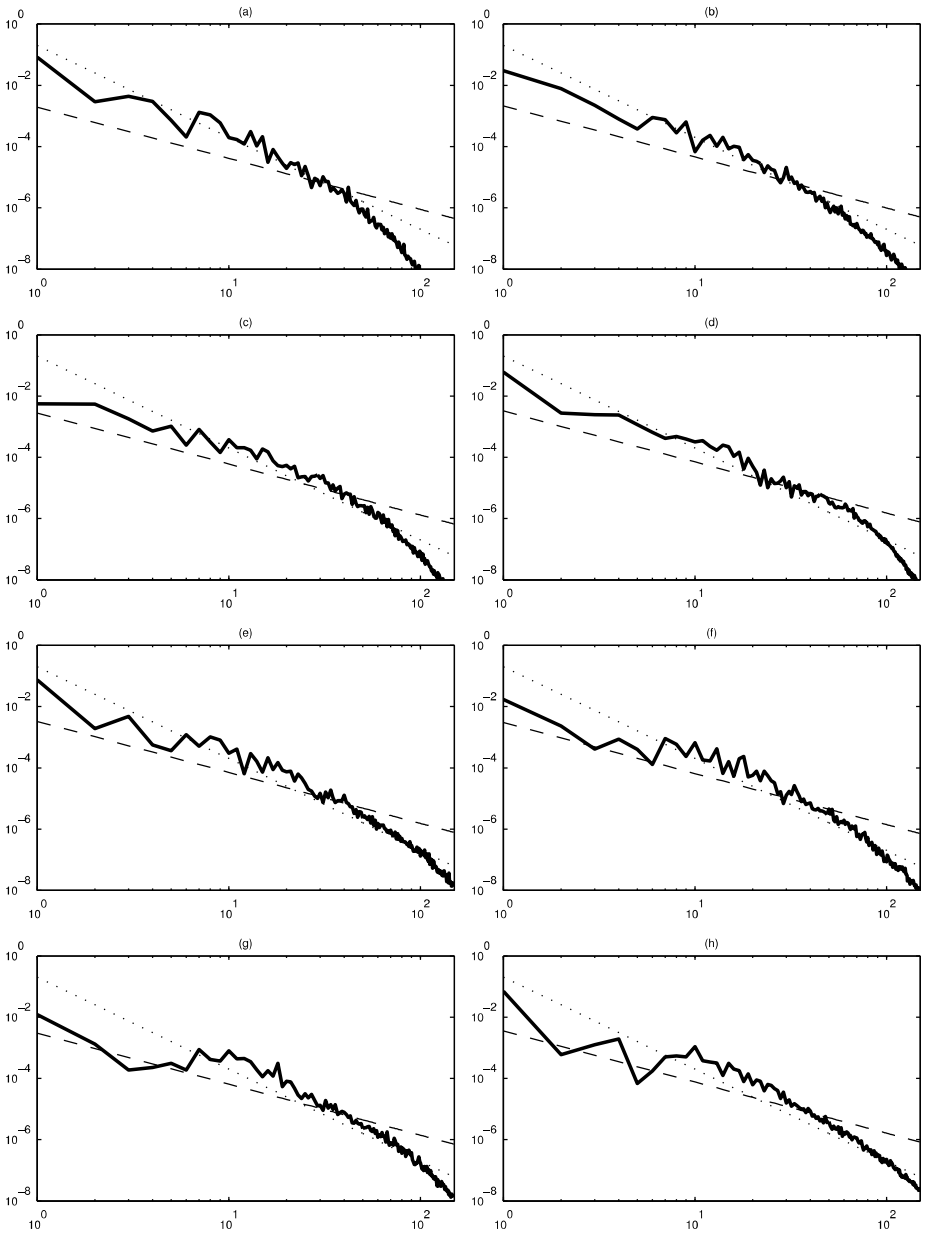

Figure 4.10: Kinetic energy spectra in the vertical direction for one linear timeperiod. First panel corresponds to $4.0T_L$, and the interval between consecutive panels is $T_L/7$. The dashed line represents the $(1/3)C_K\varepsilon^{2/3}k^{-5/3}$ inertial-range spectrum with $C_K = 1.5$ and the dotted line represents the $0.2N^2k^{-3}$ buoyancy-range spectrum.

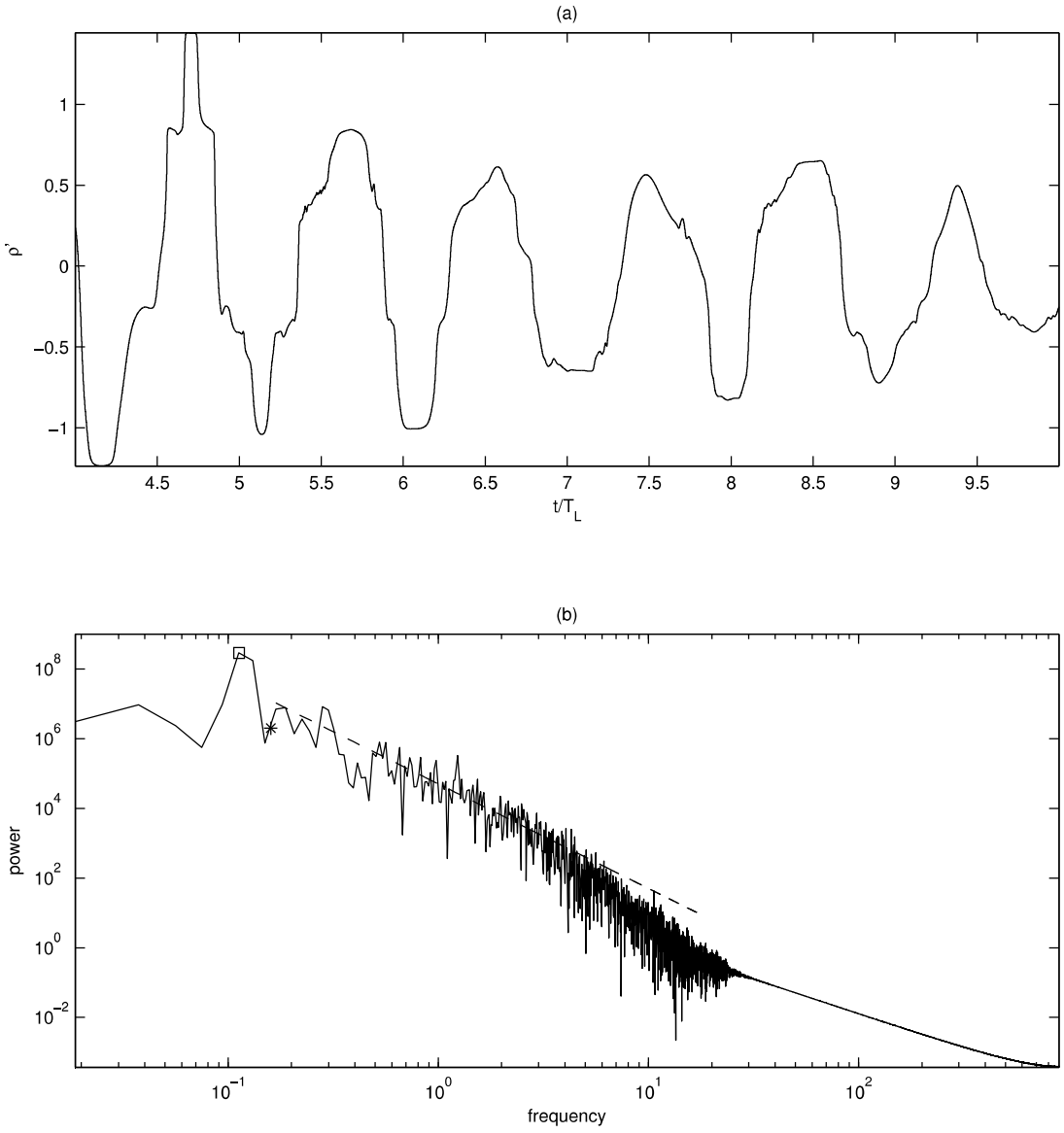

Figure 4.11: (a) The perturbation density ρ' at the center (π, π, π) of the computational domain. (b) Power spectra in logarithmic coordinates of the perturbation density. A Hamming window has been applied to the signal. The dashed line represents the f^{-3} spectrum for comparison. The buoyancy frequency $N/2\pi$ is indicated by the point *, and the frequency of the standing wave $N/(2\pi\sqrt{2})$ is indicated by the point □.

Chapter 5

Conclusions

The goal of this paper was to study the evolution of a standing internal gravity wave until breaking and overturning occurs. To do this, a code which solves the Boussinesq equations in a periodic computational cube was used. The code outputs the density and velocity fields at specified times, it also periodically outputs the kinetic and applied potential energy of the system, the dissipation rate, the kinetic energy spectra in horizontal, vertical and spherical wavenumbers, and the value of the density density field at a fixed point (taken to be the center of the domain), among other things.

We initialized the density in the computational cube to a two-dimensional standing wave, and let the code run for ten linear periods of the standing wave. We see that the wave evolves stably for about three linear time periods, after which the first breaking event happens. This is a symmetric break and the flow remains two-dimensional during the process. There is a sharp decline in the total energy of the system and an increase in the dissipation rate when the wave breaking happens. During this period, an examination of the vertical wavenumber spectra reveals a wide dissipation range and a small range of wavenumbers which align with the k^{-3} buoyancy-range spectra. The spectra and the two-dimensionality of the flow leads us to believe that turbulence is not fully developed at this point. Allowing the wave to evolve further, we observe the density field and see that another breaking event happens after about two and half linear periods. At this point, the dissipation rate has reached its maximum value and hence the Kolmogorov length scale is at a minimum. The flow has become three-dimensional and a lot of small-scale features have developed. An examination of the vertical kinetic energy spectrum shows a wide $k^{-5/3}$ inertial-range spectrum which is typical of fully developed turbulence.

The buoyancy-range spectra that we are interested in is found to be the widest in

between the two breaking events. This is because the transition from internal wave activity to turbulence is happening during this time. An examination of the frequency spectra of the density at the center of the domain reveals the f^{-3} power law to hold for frequencies higher than the internal wave frequency. This was one of the questions we were seeking to answer with this simulation, and we conclude that the use of Taylor Hypothesis in the experiments of Benielli and Sommeria [1996] is valid.

This is a surprising result, because one of the necessary conditions for the Taylor hypothesis to be valid as noted in Thorpe et al. [2007], is that the gradient of the mean relative speed $\mathrm{d}U/\,\mathrm{d}x$ is such that the smaller wavenumbers are much greater than $(2\pi\,\mathrm{d}U/\,\mathrm{d}x)/U$. In our case, the smallest wavenumber is $2\pi/L \approx 1$, and $(2\pi\,\mathrm{d}\langle w\rangle/\,\mathrm{d}x)/\langle w\rangle \approx 2\pi$ are of the same order. However, as noted in Dahm and Southerland [1997], Taylor's hypothesis is used even in conditions well outside the range of validity as envisioned by Taylor. Hence, only a DNS could justify the use of this hypothesis in the conditions of the experiments of Benielli and Sommeria [1996].

We end by noting that DNSs are hard to perform. This simulation was of a resolution 1024^3 with a Reynolds number of the order 10^4. Even a simulations resolution 4096^3, which are among the largest possible right now, would only allow us to increase the Reynolds number by a factor of 6.

APPENDICES

Appendix A

Matlab code for solving the Burgers equation

We demonstrate how the Fourier-Galerkin spectral with dealiasing using Orszag's 2/3 rule (refer Section 3.1) is applied to the viscous Burgers equation.

```
% viscosity and total time
nu=0.05; tf=1;
% grid
N=256; dx=2*pi/N; x=dx*(0:N-1);
% timestep
dt=dx/10;  nsteps=ceil(tf/dt);
% truncate at 2/3rds the largest wavenumber
cutoff = fix(N/3);
trunc = [ones(1,cutoff+1) zeros(1,N-1-(2*cutoff)) ones(1,cutoff)];
% wavenumber vectors
kx=[0:N/2-1 0 -N/2+1:-1]*1i; kx2 = kx.^2;
% initial conditions, and first timestep using Euler method
ics = sin(x); ur0 = ics; uk0 = fft(ur0).*trunc; uuk0 = fft(ur0.^2).*trunc;
uk1 = uk0 - (kx.*uuk0 - nu*kx2.*uk0)*dt;
uk1 = uk1.*trunc;

for nt = 1:nsteps
    % perform convolution in real space
    ur1 = ifft(uk1);  uuk1 = fft(ur1.^2);
```

```
    % time step using Adams Bashforth 2nd order, and truncate
    uk2 = uk1 + 0.5*dt*(3*(nu*kx2.*uk1-kx.*uuk1)-(nu*kx2.*uk0-kx.*uuk0));
    uk2 = uk2.*trunc;
    % store for next iteration
    uk0 = uk1; uk1 = uk2; ur0 = ur1; uuk0 = uuk1;
end
plot(x,ifft(uk2), 'k', x,ics,':k')
legend(['t = ' num2str(nt*dt)],'t = 0')
```

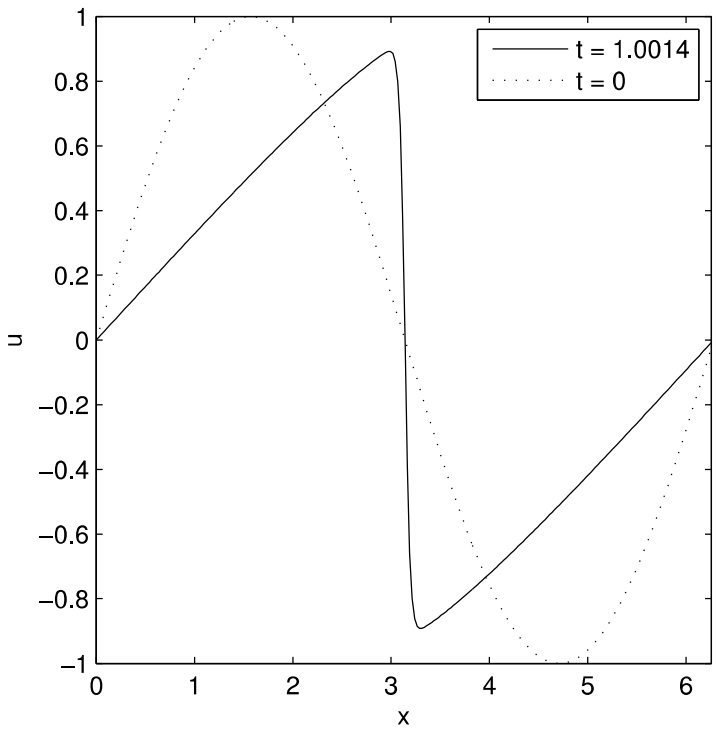

Figure A.1: Output of the above Matlab program, which solves $u_t + uu_x = \nu u_{xx}$ for $\nu = 0.05$ at $t = 1.0$ using a spectral method with dealiasing using the 2/3 rule.

References

K. Avila, D. Moxey, A. de Lozar, M. Avila, D. Barkley, and B. Hof. The onset of turbulence in pipe flow. *Science*, 333(6039):192–196, 2011.

D. Benielli and J. Sommeria. Excitation of internal waves and stratified turbulence by parametric instability. *Dynamics of atmospheres and oceans*, 23(1):335–343, 1996.

D. Benielli and J. Sommeria. Excitation and breaking of internal gravity waves by parametric instability. *Journal of Fluid Mechanics*, 374:117–144, 1998.

P. Bouruet-Aubertot, J. Sommeria, and C. Staquet. Breaking of standing internal gravity waves through two-dimensional instabilities. *Journal of Fluid Mechanics*, 285:265–301, 1995.

P. Bouruet-Aubertot, J. Sommeria, and C. Staquet. Stratified turbulence produced by internal wave breaking: two-dimensional numerical experiments. *Dynamics of atmospheres and oceans*, 23(1):357–369, 1996.

J. Boussinesq. *Théorie analytique de la chaleur: mise en harmonie avec la thermodynamique et avec la théorie mécanique de la lumière*, volume 2. Gauthier-Villars, 1903.

G. F. Carnevale, M. Briscolini, and P. Orlandi. Buoyancy-to inertial-range transition in forced stratified turbulence. *Journal of Fluid Mechanics*, 427:205–239, 2001.

W. J. Dahm and K. B. Southerland. Experimental assessment of taylors hypothesis and its applicability to dissipation estimates in turbulent flows. *Physics of Fluids (1994-present)*, 9(7):2101–2107, 1997.

P. A. Davidson. *Turbulence: An Introduction for Scientists and Engineers: An Introduction for Scientists and Engineers*. Oxford University Press, 2004.

D. R. Durran. *Numerical Methods for Wave Equations in Geophysical Fluid Dynamics/c Dale R. Durran.* Number 32. Springer, 1999.

M. Frigo and S. G. Johnson. The design and implementation of FFTW3. *Proceedings of the IEEE*, 93(2):216–231, 2005.

U. Frisch. *Turbulence: the legacy of AN Kolmogorov.* Cambridge university press, 1995.

A. Gargett, P. Hendricks, T. Sanford, T. Osborn, and A. Williams. A composite spectrum of vertical shear in the upper ocean. *Journal of Physical Oceanography*, 11(9):1258–1271, 1981.

A. E. Gill. *Atmosphere-ocean dynamics*, volume 30. Academic press, 1982.

Y. Kaneda, T. Ishihara, M. Yokokawa, K. Itakura, and A. Uno. Energy dissipation rate and energy spectrum in high resolution direct numerical simulations of turbulence in a periodic box. *Physics of Fluids*, 15(2):L21, 2003.

A. N. Kolmogorov. On the degeneration of isotropic turbulence in an incompressible viscous fluid. In *Dokl. Akad. Nauk SSSR*, volume 31, pages 319–323, 1941a.

A. N. Kolmogorov. Dissipation of energy in locally isotropic turbulence. In *Dokl. Akad. Nauk SSSR*, volume 32, pages 16–18, 1941b.

A. N. Kolmogorov. The local structure of turbulence in incompressible viscous fluid for very large reynolds numbers. In *Dokl. Akad. Nauk SSSR*, volume 30, pages 299–303, 1941c.

A. N. Kolmogorov. A refinement of previous hypotheses concerning the local structure of turbulence in a viscous incompressible fluid at high reynolds number. *Journal of Fluid Mechanics*, 13(01):82–85, 1962.

P. Kundu, I. Cohen, and D. Dowling. Fluid mechanics 5th ed, 2011.

M. Lesieur. *Turbulence in fluids*, volume 84. Springer, 2008.

S. A. Orszag. On the elimination of aliasing in finite-difference schemes by filtering high-wavenumber components. *Journal of the Atmospheric sciences*, 28(6):1074–1074, 1971.

S. A. Orszag and G. Patterson Jr. Numerical simulation of three-dimensional homogeneous isotropic turbulence. *Physical Review Letters*, 28(2):76, 1972.

L. F. Richardson. Atmospheric diffusion shown on a distance-neighbour graph. *Proceedings of the Royal Society of London. Series A, Containing Papers of a Mathematical and Physical Character*, pages 709–737, 1926.

E. Spiegel and G. Veronis. On the boussinesq approximation for a compressible fluid. *The Astrophysical Journal*, 131:442, 1960.

K. R. Sreenivasan. On the scaling of the turbulence energy dissipation rate. *Physics of Fluids (1958-1988)*, 27(5):1048–1051, 1984.

K. R. Sreenivasan. On the universality of the kolmogorov constant. *Physics of Fluids (1994-present)*, 7(11):2778–2784, 1995.

C. Staquet and J. Sommeria. Internal gravity waves: from instabilities to turbulence. *Annual Review of Fluid Mechanics*, 34(1):559–593, 2002.

G. I. Taylor. The spectrum of turbulence. *Proceedings of the Royal Society of London. Series A-Mathematical and Physical Sciences*, 164(919):476–490, 1938.

S. A. Thorpe et al. *An introduction to ocean turbulence*, volume 538. Cambridge University Press Cambridge, 2007.

M. L. Waite. Stratified turbulence at the buoyancy scale. *Physics of Fluids (1994-present)*, 23(6):066602, 2011.

M. L. Waite and P. Bartello. Stratified turbulence dominated by vortical motion. *Journal of Fluid Mechanics*, 517:281–308, 2004.